International Journal of Fatigue 161 (2022) 106918

Contents lists available at ScienceDirect

International Journal of Fatigue

journal homepage: www.elsevier.com/locate/ijfatigue

High temperature fatigue behavior of a near-alpha titanium alloy

Z. Zhao [a,*], R. Zhou [a], Z. Wang [a], J. Cai [b], B. Chen [c,*]

[a] School of Materials Science and Engineering, Beihang University, Beijing 100191, China
[b] Beijing Institute of Aeronautical Materials, Beijing 100095, China
[c] School of Engineering, University of Leicester, Leicester LE1 7RH, UK

ARTICLE INFO

Keywords:
High temperature fatigue
Very high cycle fatigue
Duality of S-N curve
Crack initiation
Primary alpha phase
Titanium

ABSTRACT

High-cycle and very-high-cycle fatigue at 450 °C in near-α titanium with bi-modal microstructure are investigated. Stress-life duality appears with one data group spanning from 10^5 to 10^7 and the other from 10^7 to 10^9 cycles, characterized by surface and subsurface cracking, respectively. Misfit strain induced by the high misorientation of a particular primary α-grain relative to its surroundings, termed as local texture, promotes the subsurface fatigue-crack initiation. Fatigue strength increases up to 100 MPa owing to cyclic pre-strain at 450 °C, but the duality remains. Strain hardening by activation of prismatic <a> slip is responsible for the improved fatigue strength.

1. Introduction

Near-α titanium alloys are designed to meet the demand for higher efficiency and weight reduction in gas turbine engines. Compared with Ti-6Al-4 V, a typical α + β alloy [1], near-α titanium alloys offer improved high-temperature performance owing to the three orders of magnitude lower self-diffusion of α-phase than β-phase [2]. The decreased β-phase fraction is achieved by increasing Sn and Zr as α stabilizing elements [3]. Meanwhile, the total content of β stabilizer is reduced together with the replacement of V by slower diffusion elements of Mo and Nb [4]. The refractory elements Mo, W, Nb and Ta are reasonable additions for high-temperature titanium (e.g. Ti-6242 [5], IMI834 [6,7] and Ti60 [8,9]) with high heat resistance [10,11] especially a good oxidation behavior [12] up to 600 °C.

IMI834 (Ti-5.8Al-4Sn-3.5Zr-0.7Nb-0.5Mo-0.35Si-0.06C, all in wt.%) has approximately 50 °C higher maximum temperature capability compared with the Ti-6242S (Ti-6Al-2Sn-4Zr-2Mo-0.1Si). Bi-modal microstructure is preferred for the application of high-pressure compressor rotors because of the low-cycle fatigue (LCF) concern. This explains why high-temperature LCF studies have inevitably focused on IMI834 with bi-modal microstructure [6,7,13-15]. Ti60 is akin to the IMI834, with increased Si concentration to improve creep resistance (0.40% in Ti60 as opposed to 0.35% in IMI834). In addition, Ti60 contains 1.5% Ta, as opposed to none in IMI834, to enhance alloy's heat resistance [10].

Compared with IMI834, high-temperature LCF work on Ti60 is rather restricted. Also, high-temperature very-high-cycle fatigue (VHCF) data is unavailable for the near-α titanium alloys. Thus, the present work is aimed to improve our understanding about the high-temperature fatigue of near-α titanium alloys, by performing LCF, high-cycle fatigue (HCF) and VHCF tests at 450 °C on Ti60 with bi-modal microstructure. The temperature of 450 °C was selected for two reasons: first, representing the typical service temperature and, second, LCF data of IMI834 in the literature [6,7,13,16] providing an important basis of our experimental design. Also, the role of oxidation on fatigue crack initiation in Ti60 at 450 °C is judged as insignificant, given that little oxide was developed at 600 °C after 100 h [17].

Duality of the stress-life (S-N) fatigue curves characterized by the two separate data groups are particularly evident in titanium alloys [18-21]. Two competing failure modes of surface versus subsurface cracking are responsible for this interesting phenomenon, with the surface-crack initiation exhibiting considerably shorter fatigue lives than the subsurface one. The subsurface cracking has been attributed to the primary α-grains as observed in fatigue tests performed at room temperature on Ti-6Al-4 V and Ti-4Al-4Mo-2Sn-0.5Si [20], two types of β titanium alloys [19], Ti-10 V-2Fe-3Al [21], and at liquid-nitrogen temperature on Ti-6Al-4 V and a near-α titanium [18].

Crystallographic facets, arising from the cleavage fracture of primary α-grains have ubiquitous influence on the fatigue-crack initiation in α + β, near-α and β titanium alloys at room temperature. Two examples are highlighted here. First, the origin of subsurface fatigue cracking in Ti-6Al-4 V over the VHCF regime of 10^7 to 10^9 cycles, has been attributed

* Corresponding authors.
E-mail addresses: zhzh@buaa.edu.cn (Z. Zhao), bo.chen@leicester.ac.uk (B. Chen).

https://doi.org/10.1016/j.ijfatigue.2022.106918
Received 30 November 2021; Received in revised form 1 March 2022; Accepted 10 April 2022
Available online 12 April 2022

to the transgranular fracture of primary α-grain or a cluster of α-grains (i.e. microstructural inhomogeneity) [22-26]. Second, subsurface fatigue crack initiation in Ti-6242 was associated with the primary α-grain facets [5,27]. However, the role of primary α-grains on fatigue-crack initiation of titanium including the near-α type in the HCF and VHCF regimes at elevated temperatures has been barely studied.

Here, the duality of S-N curve on Ti60 at 450 °C in the HCF/VHCF life regime of 10^5 to 10^9 cycles was studied. This was followed by investigating the effect of cyclic pre-strain at 450 °C on the subsequent HCF/VHCF properties at the same temperature. Note that all the HCF/VHCF data were generated using the ultrasonic fatigue tester. Quantitative fractography and microstructure observations were performed using a range of complementary characterization tools, to elucidate the underlying mechanisms that control deformation, crack initiation and the overall fatigue life.

2. Experimental

2.1. Material and tensile properties

Ti60, a high-temperature near-α titanium, belongs to the Ti-Al-Sn-Zr alloy series. The Ti60 was supplied by BIAM, China, in a multi-step forged and fully heat-treated condition. The bi-modal microstructure was characterized by primary α-grains (referred to as α_p) with the volume fraction of 23.5%, embedded in a lamellar transformed β-matrix (T_β), as shown in Fig. 1a. The lamellar matrix was characterized by the colony size of 63.2 ± 8.9 μm with alternating α plates and thin β lamellae, see the inset of Fig. 1a. The size distribution of α_p-grains is presented in Fig. 1c, from which the average size was determined as 40.9 ± 12.5 μm. The clustering of the α_p-grains with a longitudinal chain-like feature (termed as cluster defect), as reported by Ravi Chandran and Jha [21] on Ti-10 V-2Fe-3Al, was not found in the present Ti60.

Electron backscattered diffraction (EBSD) inverse pole figure IPF-TD map of the as-received Ti60 is shown in Fig. 1b; refer to Fig. 6g for the coordinate system. The corresponding pole figure is presented in the inset of Fig. 1c, revealing a relatively weak overall texture with the multiple of uniform density (mud) of 6.8 as a maximum. The overall texture in T60 is claimed to be low especially when compared with the strong overall texture (16.15 mud) in Ti-600 [28]. Throughout the present paper, the overall texture is derived from the EBSD analysis covering >700 grains, whilst the phrase of local texture is used to indicate the region that particularly relates to the crack initiation including less than 10 grains. When the phrase of individual grain orientation is used, it emphasizes the high misorientation angle of the α_p-grain with respect to its surroundings as identified within the fatal-crack initiation region.

The Ti60 chemical composition is summarized in Table 1 and compared with the IMI834 [7], with the key difference being the content of Ta and Mo. Ta is a typical β-phase stabilizer (Mo equivalent content of 0.28) [4], and its diffusion coefficient at 600 °C is one tenth of the self-diffusion of α-Ti. The Ti60 is known to exhibit good creep properties with plastic strain of ≤ 0.09% when tested at 600 °C, 150 MPa and 100 h [10].

Table 1
Chemical compositions of Ti60 (in wt.%) and IMI834 near-α titanium alloys.

Alloy	Al	Sn	Zr	Nb	Ta	Mo	Si	C	Ti
Ti60	5.8	4.0	4.0	0.7	1.5	N/A	0.40	0.06	Bal.
IMI834	5.8	4.0	3.5	0.7	N/A	0.5	0.35	0.06	Bal.

Tensile tests at 450 °C were performed using an MTS-810 tester equipped with electric resistance furnace. Tensile specimen made of Ti60 had a gauge length of 60 mm and diameter of 5 mm (Fig. S1). Three individual tests were conducted to obtain the average yield strength of 680.0 MPa, ultimate tensile strength of 692.1 MPa, elongation-to-failure of 28.8%, and Young's modulus of 73.0 GPa.

2.2. Low-cycle and very-high-cycle fatigue testing

LCF tests were conducted at 450 °C in air using MTS-50KN-1 machine with strain-controlled triangular load waveform under a frequency of 0.25 Hz. The LCF specimen had dimensions of 15 mm in gauge length and 7 mm in diameter (Fig. 2a). An extensometer was attached within the gauge section to monitor the axial strain. The strain amplitudes ($\Delta\sigma/2$), ranging from ±0.5% to ±1.0%, were employed to generate LCF data, allowing us to understand the cyclic stress response of Ti60 at 450 °C in comparison with IMI834.

Both the ±0.6% and ±0.8% strain amplitudes were considered further for generating cyclic pre-strained Ti60, given that the fatigue life of ±0.5% specimens exceeded 10^4 cycles (towards the HCF regime) with limited cyclic hardening, while the ±1.0% specimen had a very short fatigue life of 644 cycles, Fig. S2. The cyclic pre-strain experiments with predefined fatigue cycles, equivalent to 10% and 20% of the LCF life, under the respective ±0.6% and ±0.8% strain amplitudes, were then conducted. More details about the high-temperature LCF testing can be found elsewhere [29,30].

Ultrasonic fatigue testing was conducted on a Shimadzu USF-2000 instrument to study the effect of cyclic pre-strain on HCF and VHCF properties at 450 °C. All tests were performed under fully reversed loading (i.e. stress ratio of $R = -1$) at a frequency of 20 kHz. The stress amplitude ranged from 265 to 330 MPa to generate the S-N data in the fatigue lifetime from 10^5 to 10^9 cycles. The specimen was heated using induction coils integrated with a closed-loop temperature controller. An infrared thermometer was used to monitor the surface temperature to ensure the test temperature within ±3 °C with reference to 450 °C.

For the specimens that had received a predefined level of cyclic pre-

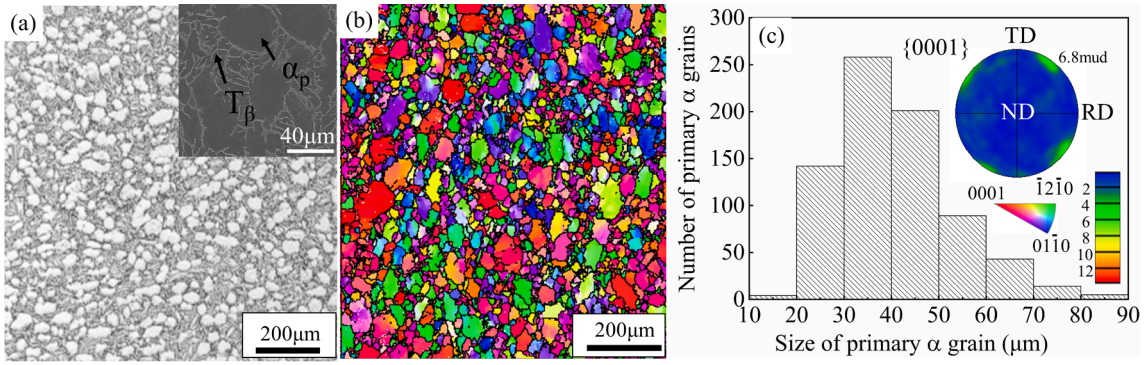

Fig. 1. Ti60 microstructure in as-received condition: (a) optical micrograph and scanning electron micrograph showing the primary α-grains embedded in a lamellar transformed β-matrix; (b) electron backscattered diffraction (EBSD) IPF-TD map; (c) size distribution of primary α-grains. For metallography in (a), chemical etching was made in a solution of 2% HF, 6% HNO_3 and 92% H_2O. The inset in (c) is the pole figure created from the EBSD map in (b).

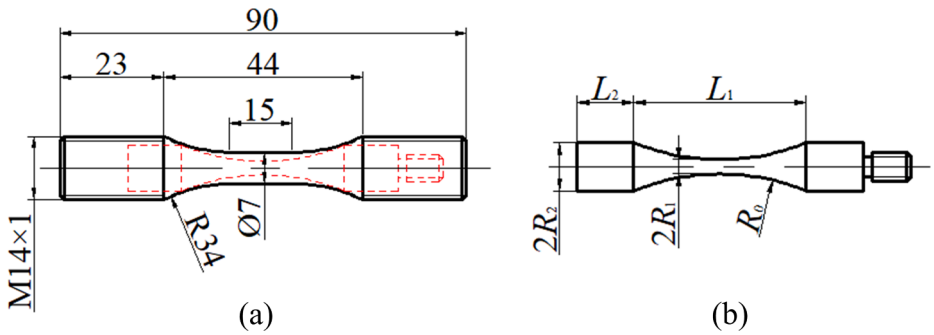

Fig. 2. (a) LCF specimen dimension; (b) specimen dimension for the ultrasonic fatigue testing to generate HCF/VHCF data in both the cyclic pre-strained and no pre-strained conditions.

strain at 450 °C, they were machined to VHCF specimens as shown in Fig. 2b. No pre-strained VHCF specimens were extracted directly from the as-received Ti60. The specimen radius, $R_1 = 1.5$ mm and $R_2 = 5.0$ mm, and length of $L_1 = 18$ mm were used. The specimen was axisymmetric with a reduced section at the center, and the end length L_2 was calculated as 11.8 mm by using dynamic elastic modulus of $E_d = 121$ GPa and material density of $\rho = 4.6$ g/cm^3. The value of $R_0 = 48.04$ mm was then worked out. All specimens were prepared down to a surface finish with Ra value of 1.6 μm. More details about the VHCF specimen design and the instrument set up can be found in [31-33].

2.3. Post-mortem examination

Fracture surface of the post-fatigued specimen was examined under a Zeiss Supra-55 field-emission-gun scanning electron microscope (SEM) by using secondary electron. The SEM fractography included all LCF, HCF and VHCF specimens, with particular emphasis to identify the crack initiation characteristics. Energy-dispersive X-ray spectrometry (EDS) was used to determine chemical compositions semi-quantitatively at the initiation site.

Microstructure and texture information from the post-fatigued specimens were acquired using electron backscattered diffraction (EBSD). The EBSD scan over a large field-of-view, containing > 700 primary α-grains per sample was performed at 20 kV with step sizes from 0.2 to 2.5 μm. Procedures of the longitudinal cross-section, EBSD sample preparation and its data post-processing can be found in [34-37].

Transmission electron microscopy (TEM) was performed using a JEM-2100 high-resolution microscope at 200 kV. The bright-field imaging mode together with selected area diffraction (SAD) was used to understand the deformation mechanisms. TEM specimens were cut from the location within 2 mm distance to the fracture surface, followed by mechanical polishing down to 50 μm and then Ar + ion milling to electron transparency on a Gatan PIPS II system. SAD patterns were processed using Digital Micrograph to index all the diffraction spots [38].

3. Results

3.1. HCF and VHCF baseline data

Fig. 3 presents the Ti60 fatigue S-N data ranging from 6.79×10^4 to 1.00×10^9 cycles. 33% of specimens were cracked from the surface whereas 67% from the subsurface, and the transition between the two initiation modes occurred at 10^7 cycles. Fig. 4a presents a typical SEM fractography of the specimen ($N_f = 6.55 \times 10^6$) with surface fatigue cracking, revealing no distinct feature for the crack initiation region. By contrast, the subsurface crack initiation site with ~ 800.0 μm distance to the surface seemed to be rougher in Fig. 4b, suggesting the presence of localized plastic deformation for the specimen with a longer fatigue life of $N_f = 3.30 \times 10^8$. The rough zone had an equivalent diameter of

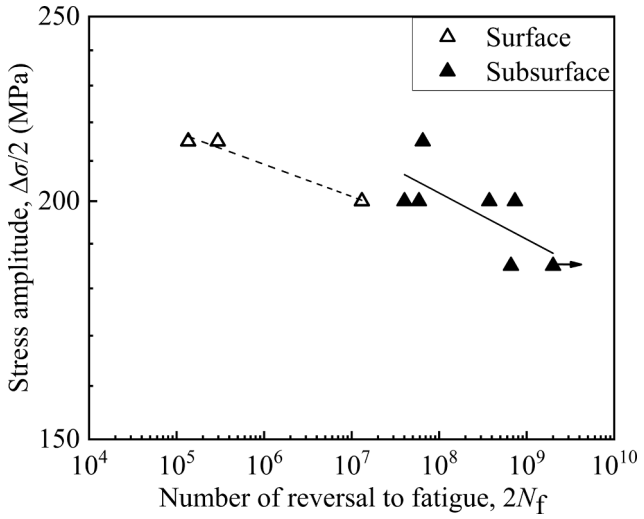

Fig. 3. HCF and VHCF baseline fatigue S-N data of Ti60 at 450 °C. All tests were performed under $R = -1$ at 20 kHz. Symbol with arrow indicates fatigue run-out.

1113.8 μm. Chemical composition of the rough zone was analyzed by EDS, revealing no compositional difference, Fig. S3. Two additional SEM fractography are given in Fig. S4 to verify that the specimen failed with longer fatigue life is characterized by the subsurface fatigue-crack initiation with the rough zone.

Longitudinal cross-section was performed on the fracture surface to allow investigation of the initiation site underneath. Fig. 5a presents the subsurface fatigue cracked specimen, while that characterized by the surface cracking is illustrated in Fig. 5c. For the subsurface cracked Ti60, the initiation region was characterized by a primary α-grain with equivalent diameter of 39.4 μm, Fig. 5b. Note that the cross-sectional view in Fig. 5b represented only part of the fractured primary α-grain, suggesting that the fatal-crack initiation might be due to a slightly larger α-grain than the average size, located in the subsurface. By contrast, the fatigue specimen failed with surface cracking did not reveal the fracture of a similar sized primary α-grain, Fig. 5d.

Fig. 6 presents the cross-sectional EBSD results with the subsurface cracked specimen in Fig. 6a and 6b, while those associated with the surface cracking in Fig. 6c to 6f. The α-phase fraction was measured to be > 93%, and hence both the pole figure and IPF-TD orientation maps were derived from the α-grains. Fig. 6g presents the EBSD coordinate system where TD, RD and ND indicate transverse, radial and normal directions, respectively, and the fatigue loading axis is parallel to the TD. The EBSD scan was made on the TD-RD plane, with the left side indicating the specimen surface and TD being the vertical direction.

For the subsurface cracked Ti60, the primary α-grain of fatal-crack

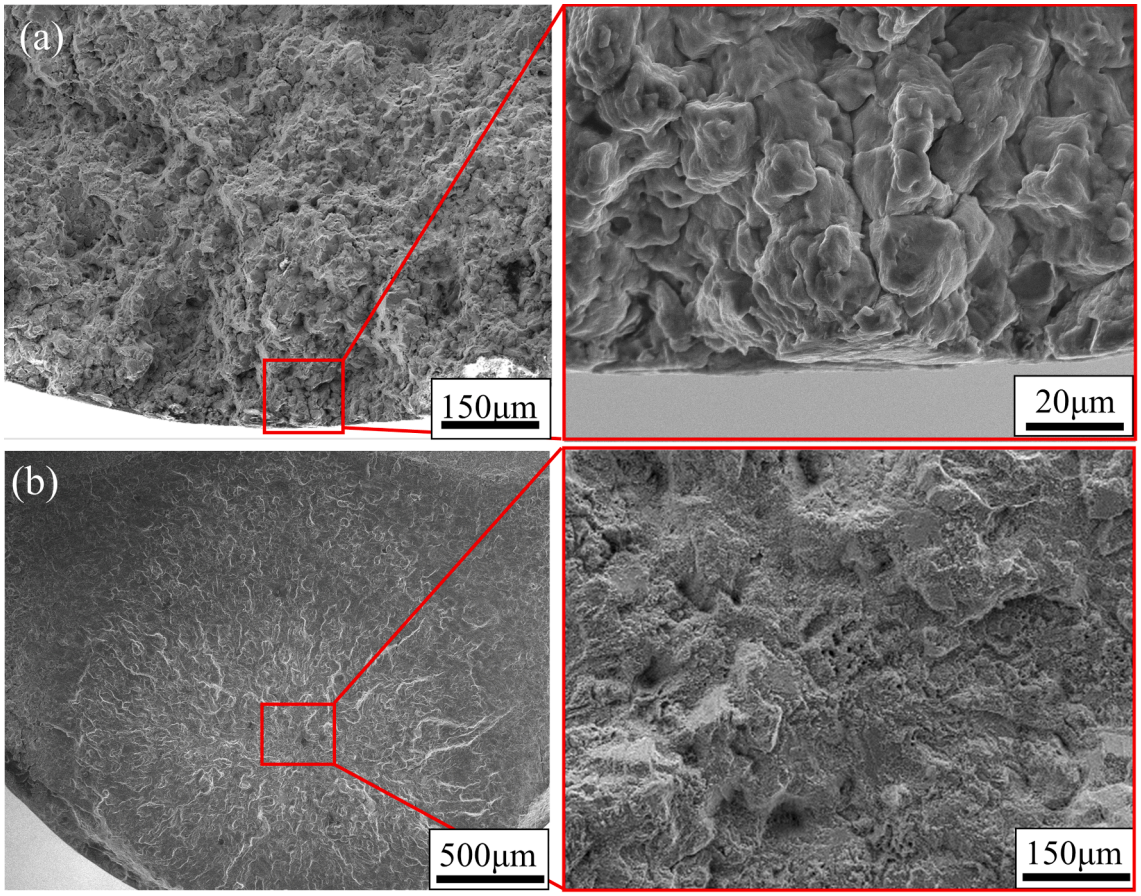

Fig. 4. SEM fractography of no pre-strained Ti60 specimens: (a) Surface fatigue-crack initiation, σ_a = 200 MPa, N_f = 6.55 × 10^6; (b) Subsurface fatigue-crack initiation, σ_a = 185 MPa, N_f = 3.30 × 10^8.

initiation (indicated by letter A in Fig. 6a) had its c-axis nearly perpendicular to the loading axis. For such an orientation, the basal < a > slip would be less likely activated than the prismatic < a >. For the neighboring grains 1 to 6 in Fig. 6a, the grain-to-grain misorientation angle with reference to grain A, was measured to be 81.1°, 31.7°, 81.8°, 80.7°, 86.8° and 82.0°, respectively. This suggests that strain incompatibilities existed between the cracked α-grain and the surrounding regions. The overall texture of the subsurface cracked Ti60 was weak (4.5 mud as a maximum in Fig. 6b). By excluding the crack initiation region, the value changed to 4.6 mud, virtually the same as that including all regions.

For the surface cracked Ti60, the overall texture was considerably high (13.5 mud in Fig. 6d), and the basal pole was oriented at 75° relative to the loading axis. Interesting to note, the cracked α-grain (grain A in Fig. 6c) had its c-axis nearly perpendicular to TD, whereas its surrounding grains had their c-axis parallel to it, with the misorientation angles from 60.0 to 85.0°. Additionally, all the grains subjacent the fatigue-crack initiation site (Fig. 6c) were very small with the size of 2.2 ±1.8 μm. Note that the fine-grained region was also seen at the specimen surface, Fig. 6e (IPF-TD map) and 6f (band contrast map). These fine grains with random orientations can be attributed to surface recrystallisation at 450 °C. Note that the fine grains as revealed at the fracture surface had little effect on the overall texture, due to the chosen step size of 2.5 μm for the whole area (Fig. 6c) while 0.2 μm for the crack initiation region (the figure inset).

Furthermore, two large α-grains were located just beneath the fine-grained region of fatal-crack initiation, Fig. 6c. They contained several α plates, separated by high-angle grain boundaries (HAGBs defined by > 10° misorientation), with the c-axis parallel to fatigue loading. By using the coincidence site lattice (CSL) for the hcp structure [34,39], the Σ11a, Σ13a and Σ24 type boundaries were found to be predominant with their respective fractions of 5.2%, 5.2% and 4.3% in the post-fatigued Ti60. They should not be interpreted as deformation twins, given that their rotation axis of [10$\bar{1}$0] coupled with the misorientation angle (84.8°, 85.6°, 85.2° for Σ11a, Σ13a and Σ24, respectively) does not align with any of the commonly identified twin types [40,41].

3.2. Cyclic pre-strain

Fig. 7a shows the cyclic stress amplitude ($\Delta\sigma/2$) versus plastic strain amplitude ($\Delta\varepsilon_p/2$) as determined from the saturated hysteresis loops at the half-life of the LCF tests at 450 °C. The relationship between $\Delta\sigma/2$ and $\Delta\varepsilon_p/2$ can be described with the power law function of $\Delta\sigma/2 = K'(\Delta\varepsilon_p/2)^{n'}$. The least squares regression analysis performed on their bi-logarithmic plot in Fig. 7a, returned the values of K'=776.25 MPa and n'=0.05 for Ti60. By comparison with the 450 °C LCF data of IMI834 in [13], Ti60 had a lower cyclic hardening capability.

It is known that the LCF life is determined by the plastic strain amplitude ($\Delta\varepsilon_p/2$). The Coffin-Manson model that correlates the number of reversals to failure ($2N_f$) with the $\Delta\varepsilon_p/2$ using a power law relation of $\Delta\varepsilon_p/2 = \varepsilon_f'(2N_f)^c$ has thus been chosen, with ε_f' and c termed as fatigue ductility coefficient and fatigue ductility exponent, respectively. The LCF life of Ti60 decreased with the increasing plastic strain amplitude, Fig. 7b. Such a relationship can be predicted reasonably well by using the Coffin-Manson model, and the characteristic parameters of ε_f' and c were determined as 16.98 and −1.16. Overall, Ti60 exhibited a comparable LCF life with that of IMI834 at 450 °C.

For the two considered strain amplitudes (±0.6% and ±0.8%), the cyclic stress response curves for the Ti60 are shown in Fig. 7c in comparison with IMI834. Both materials exhibited cyclic softening over the

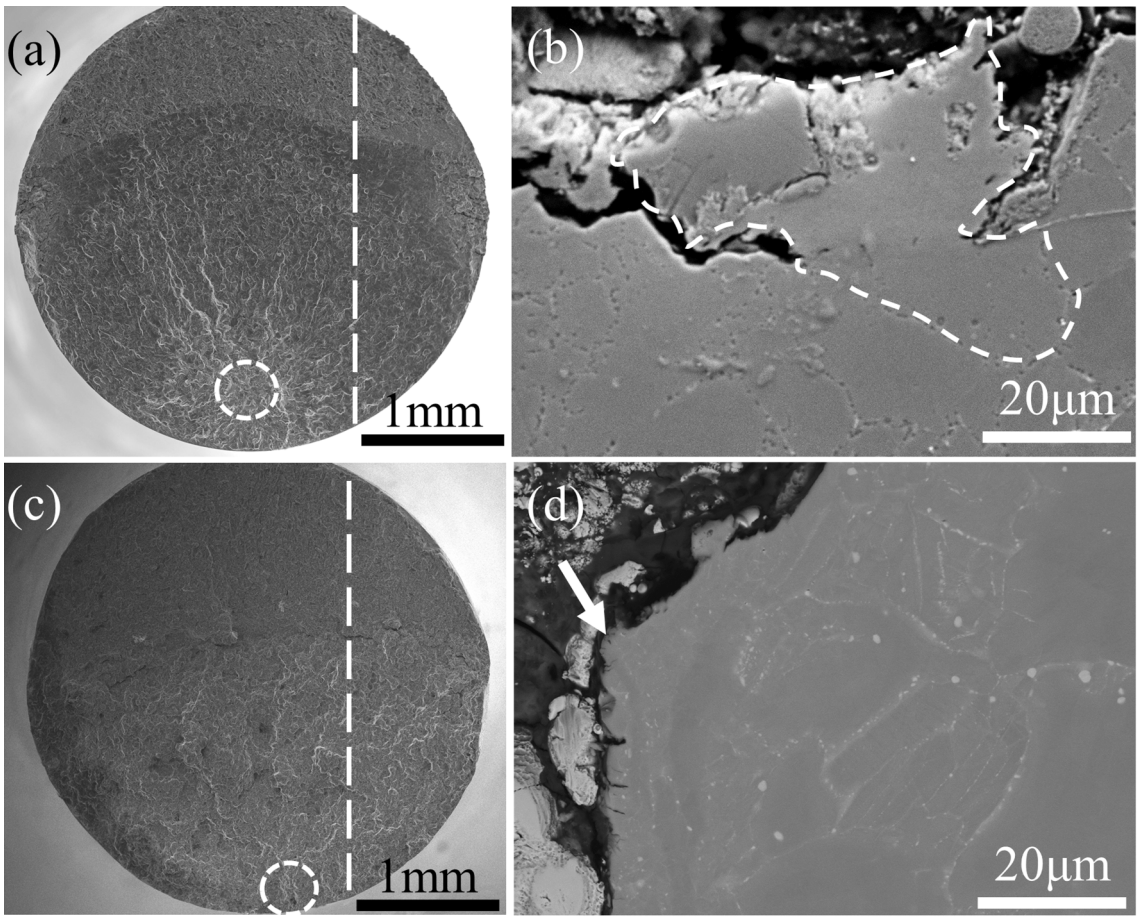

Fig. 5. (a) and (c) SEM fractography of the subsurface and surface fatigue-crack initiation, respectively, with the circle indicating the fatal-crack initiation region and the dashed line indicating sectioning followed by grinding towards the initiation region; (b) and (d) SEM longitudinal cross-sectional view. (a) and (b) specimen tested at $\sigma_a = 215$ MPa, $N_f = 3.25 \times 10^8$; (c) and (d) specimen tested at $\sigma_a = 200$ MPa, $N_f = 6.55 \times 10^6$. Arrow in (d) indicates the surface crack initiation region, while the dashed outline indicates the primary α-grain that triggers the subsurface cracking.

initial 10 cycles, followed by the cyclic hardening. This observation applies to both strain amplitudes. The higher strain amplitude of ±0.8% led to higher tensile peak stress σ_p, but shorter LCF life N_f. It is evident that the IMI834 had stronger cyclic hardening than Ti60, despite little difference in their LCF life. Fig. 7d presents the Ti60 hysteresis loops determined from the half-life cycle of the ±0.6% and ±0.8% strain amplitudes (two for each condition). The tensile phase had a lower stress level compared to the compressive phase. The average hysteresis loop area was measured to be 1.34 MJ/m^3 for the ±0.6%, while 3.93 MJ/m^3 for the ±0.8%, indicating a higher plastic strain in the latter. Since the two specimens per strain-amplitude condition showed a reasonably good consistency, their respective average fatigue lives of 2798 (±0.6%) and 1155 (±0.8%), were then used for calculating the required cycles to achieve the intended cyclic pre-strain conditions. This resulted in the interrupted fatigue cycles of 280 (10% of the LCF life) and 360 (20%) for the ±0.6% strain amplitude, while 116 (10%) and 232 (20%) for the ±0.8% counterpart.

Representative cyclic stress response curves of the ±0.6% and ±0.8% pre-strained specimens (two from each condition) are shown in Fig. 8a, and the corresponding hysteresis loops as determined from the last registered cycle are illustrated in Fig. 8b. At ±0.6% strain amplitude, the tensile peak stress of the Ti60 that received a pre-strain of 10% of the LCF life was found to be 500.6 MPa, which is lower than that of 519.8 MPa for the 20% counterpart. A similar trend can be seen for the ±0.8% strain amplitude, namely, 542.9 MPa for the 10% while 561.9 MPa for the 20% of the LCF life. The hysteresis loop areas (Fig. 8b) were measured to be 1.17 MJ/m^3 and 1.19 MJ/m^3 for ±0.6% specimens, while 3.95 MJ/m^3 and 4.02 MJ/m^3 for ±0.8% ones.

All the LCF specimens (450 °C, R = -1, 0.25 Hz) were failed by surface cracking, namely, the fatal fatigue crack initiated on the surface of the specimen. A representative SEM fractography is presented in Fig. 9a. This finding is consistent with the previous work on various titanium alloys including TA15, Ti-24Nb-4Zr-8Sn and Ti-2Al-2.5Zr [42-44]. Based on the LCF hysteresis loops, the tension- and compression-going elastic moduli were calculated, respectively, for selected fatigue cycles. The difference between the two appeared to increase exponentially after 2000 and 1000 cycles, as illustrated in Fig. 9b for the ±0.6% and ±0.8% test conditions. This implies that the fatigue crack most likely developed after 80% of the LCF life. Therefore, the potential effect of surface cracking developed during the cyclic pre-strain (10% and 20% of the LCF life) on the subsequent VHCF behavior is judged to be negligible. Also, it is important to mention that even if some shallow surface cracks were generated in the cyclic pre-strained Ti60, they would have been removed during the VHCF specimen machining stage (see Fig. 2).

3.3. HCF and VHCF behavior of cyclic pre-strained Ti60

Fig. 10 compares the HCF and VHCF fatigue behavior of the cyclic pre-strained Ti60 with that receiving no pre-strain. The dataset was generated using the ultrasonic fatigue tester with the different stress amplitudes ranging from 265 MPa to 330 MPa. The fatigue strength coefficient σ_f' and exponent b were worked out by fitting the S-N curves with the Basquin equation $\Delta\sigma/2 = \sigma_f'(2N_f)^b$, where $\Delta\sigma/2$ is the stress

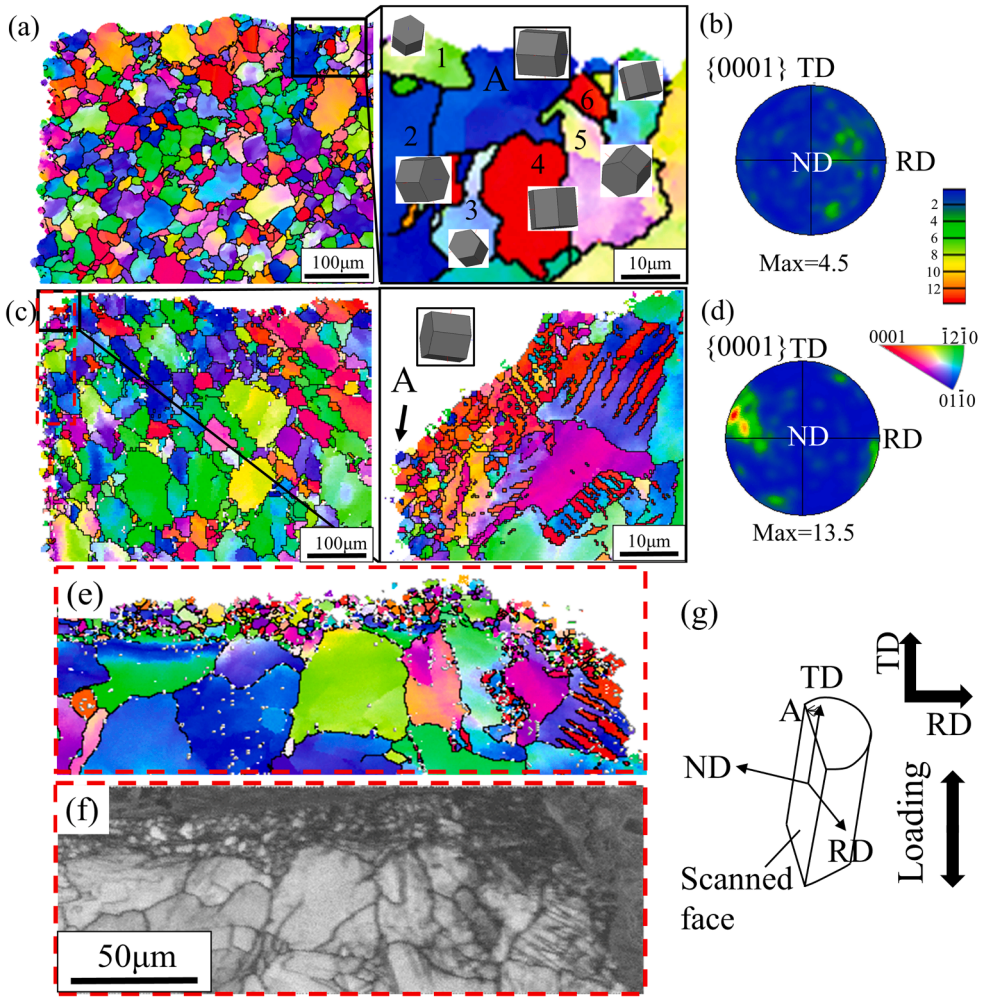

Fig. 6. EBSD cross-sectional observation of the post-fatigued Ti60 that had not been subjected to cyclic pre-strain: (a) subsurface fatigue-crack initiation, $\sigma_a = 200$ MPa, $N_f = 3.67 \times 10^8$; (c) surface fatigue-crack initiation, $\sigma_a = 200$ MPa, $N_f = 6.55 \times 10^6$. (a) and (c) IPF-TD maps; (b) and (d) {0001} pole figures; (e) and (f) IPF-TD map showing the fine-grained surface region and the corresponding band contrast map with HAGBs defined with misorientation angle of > 10 deg; (g) schematic diagram showing the EBSD coordinate system with reference to the fatigue loading.

amplitude. The HCF/VHCF properties are summarized in Table 2, which provides quantitative description about the beneficial effect of cyclic pre-strain on fatigue strength of Ti60.

Several interesting phenomena can be seen in Fig. 10. First, fatigue life increased due to cyclic pre-strain, with the strength enhancement of ~ 100 MPa. Second, the S-N duality characteristics (surface fracture with low N_f as opposed to subsurface fracture with high N_f) remained. Third, the fatigue dataset did not reveal any quantifiable difference between the 10% and 20% of the LCF life, nor for the ±0.6% and ±0.8% strain amplitudes. Fourth, for the cyclic pre-strained Ti60, 49% of specimens failed from the surface, while 51% from the subsurface, based on the total number of thirty-seven HCF/VHCF tests including one fatigue run-out. This seems to suggest that the cyclic pre-strain can increase the Ti60 propensity to surface cracking. Further study is required to clarify this because the number of fatigue tests performed on the no pre-strained Ti60 (Fig. 3) was significantly lower than the pre-strained ones.

SEM fractography in Fig. 11, taken from four representative specimens failed with either the surface or subsurface cracking. The white outline indicates the identified fatigue-crack initiation region. In total, 15 fatigue specimens were fractured by the surface cracking, with 3 of them exhibiting a distinctive crack-initiation region characterized by the rough zone, Fig. 11b. The rest of 12 specimens (representing 75% of the surface cracked specimens) revealed little difference between the crack-initiation region and its surrounding areas, Fig. 11a, Fig. S5a and S5c. By contrast, all the subsurface cracked specimens (12 specimens in total) exclusively showed a distinctive rough zone, Fig. 11c and 11d as well as Fig. S5b and S5d. The equivalent diameter of the rough zone was measured to be 142.4 μm (Fig. 11c) and 123.6 μm (Fig. 11d) for the subsurface cracked specimens with the fatigue life of $N_f = 3.02 \times 10^7$ and $N_f = 1.80 \times 10^8$, respectively. The distance of the rough zone to the specimen surface was found to be 74.3 μm and 118.9 μm, respectively. Longitudinal cross-sections were prepared using the same approach as illustrated in Fig. 5a and 5c. The primary α-grain facet of 32.8 μm in diameter, slightly smaller than the average grain size of 40.9 ± 12.5 μm, was responsible for the fatal-crack initiation from the subsurface, Fig. 12a. By contrast, no evidence suggested a similar sized primary α-grain facet leading to the surface fatigue cracking, Fig. 12b.

Fig. 13a and 13b present the IPF-TD map and {0001} pole figure for the cyclic pre-strained Ti60 that was characterized by the subsurface fatigue cracking, while Fig. 13c to 13f for the surface fatigue cracking. The overall texture of the cyclic pre-strained Ti60 was relatively weak, regardless of cracking characteristics (subsurface in Fig. 13b vs. surface in Fig. 13d). But some seemingly strong and localized basal texture can be seen from the IPF-TD map, Fig. 13a and 13c. For the subsurface initiation, the fatal cracked primary α-grain (grain A in Fig. 13a) had a distinctive orientation when compared to its adjacent grains, with the grain-to-grain misorientation determined to be 67.1°, 68.2°, 55.8° and 45.1°, respectively. Interesting to note, grain A had its c-axis nearly parallel to the TD, suggesting a lower possibility for the < a > slip activation. For the surface cracked specimen, the primary α-grain of fatal-crack initiation had its c-axis tilted with 15° to TD, and again the grain-to-grain misorientation with its surrounding was high, with the value ranging from 60.0° to 89.0°. The combined IPF-TD and band

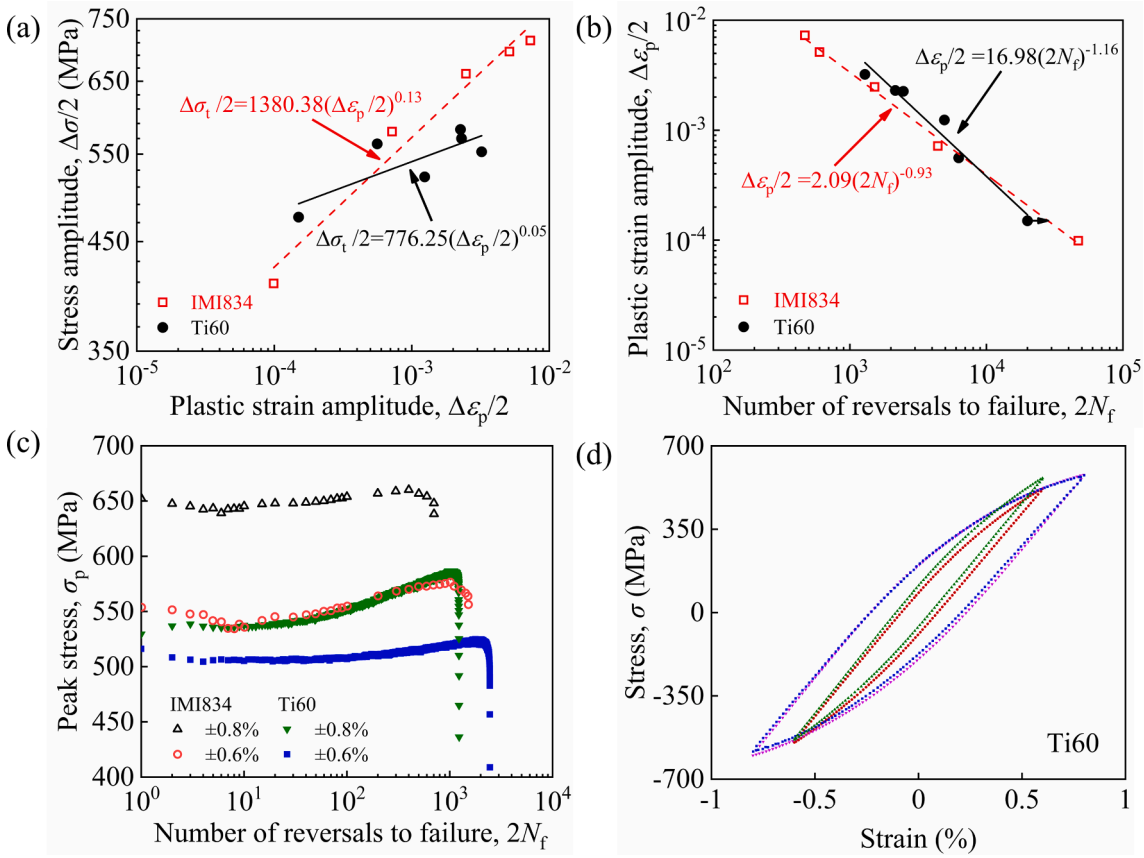

Fig. 7. (a) Stress amplitude ($\Delta\sigma/2$) versus plastic strain amplitude ($\Delta\varepsilon_p/2$); (b) Coffin-Manson plots of the plastic strain amplitude ($\Delta\varepsilon_p/2$) versus number of reversals to failure ($2N_f$) obtained from the LCF data of Ti60 and IMI834 under different strain amplitudes; (c) cyclic stress response curves of the Ti60 and IMI834; (d) hysteresis loops at half-life cycle for the strain amplitude of ±0.6% and ±0.8% of Ti60. Note the IMI834 data were taken from [13].

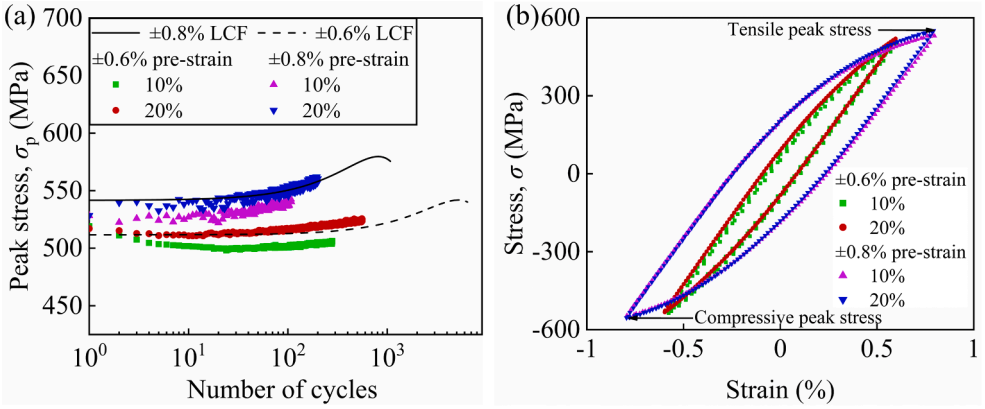

Fig. 8. Representative cyclic stress response curves in (a) and hysteresis loops in (b) at the fatigue cycles corresponding to 10% and 20% of the LCF life.

contrast maps in Fig. 13e and 13f confirmed no surface fine-grained region in this case.

4. Discussion

4.1. Roles of primary α-grain size and location, test frequency and oxidation

In this work, the behavior of crack initiation in HCF and VHCF regimes at 450 °C in Ti60 with bi-modal microstructure is studied. One specimen group with shorter fatigue life of $N_f < 10^7$ is characterized by the surface cracking, while the other having longer life of $N_f > 10^7$ is characterized by the subsurface cracking, Fig. 10. The S-N curve duality was also found at room-temperature fatigue of Ti-6246 [45], where the surface cracking dominated at higher stress amplitude, whereas an increased competition between surface and subsurface cracking appeared at lower stress amplitude. By performing fatigue testing on Ti-10V-2Fe-3Al and Monte-Carlo simulations based on Poisson defect statistics, Ravi Chandran and Jha [21] related the probability of surface vs. subsurface cracking to the occurrence probability of clusters of primary α-grains at the surface. The shorter fatigue life was thus attributed to the presence of these α-grain clusters at the specimen surface. Obviously, the present Ti60 exhibits a homogenous bi-modal microstructure, Fig. 1, i.e. without showing any α-grain clusters. In addition, the observed S-N

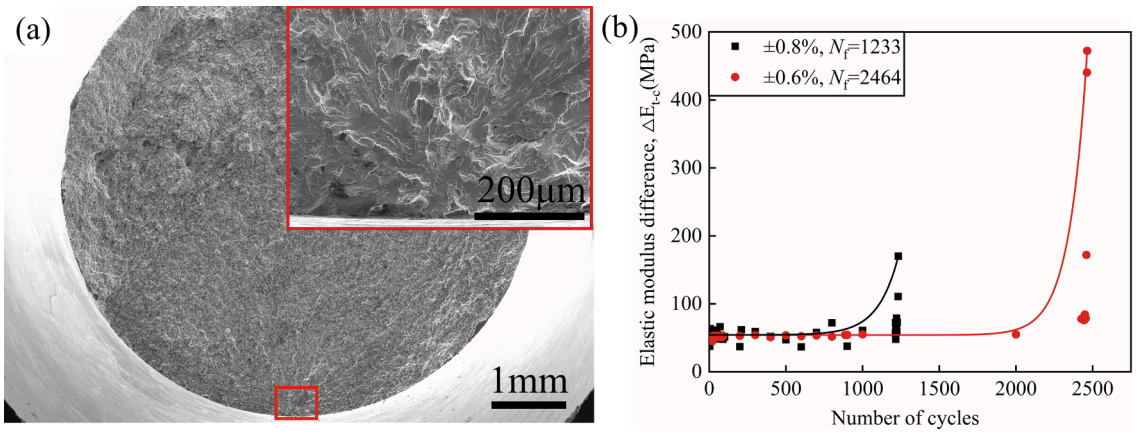

Fig. 9. (a) A representative SEM fractography of the LCF sample (strain amplitude of ±0.6%, N_f = 3131); (b) the difference between the tensile and compressive elastic moduli for the two LCF samples.

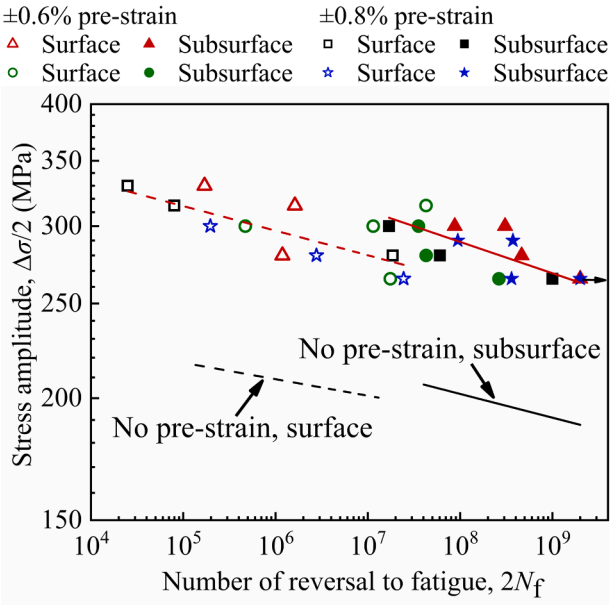

Fig. 10. Comparison of the HCF and VHCF fatigue S-N data at 450 °C between the cyclic pre-strained and no pre-strained conditions. For the no pre-strained Ti60, only the data fitting lines from Fig. 3 are given here to reduce unnecessary confusion. All tests were performed under R = -1 at 20 kHz.

Table 2
HCF/VHCF fatigue properties of pre-strained vs. no pre-strained Ti60.

Material condition	Crack initiation site	Fatigue strength coefficient σ_f (MPa)	Fatigue strength exponent b
Cyclic pre-strain	Surface	416.87	−0.025
	Subsurface	524.81	−0.032
No pre-strain	Surface	263.03	−0.017
	Subsurface	316.23	−0.024

curve duality was kept in the cyclic pre-strained Ti60, despite enhanced fatigue strength due to pre-straining, Fig. 10.

In α + β titanium alloys, fatigue crack formation is primarily crystallographic and strongly influenced by the microstructural inhomogeneity such as the size and distance to specimen surface, as well as the orientation of primary α-grains [21-23,26,45-47]. Heinz and Eifler [22] reported that micro-cracks were developed in larger primary α-grains in Ti-6Al-4 V in the VHCF regime at room temperature, leading to the subsurface fatigue failure. Szczepanski et al. [45] also commented that the primary α-grain in Ti-6246 that promoted the facet formation by transgranular fracture during room-temperature VHCF was typically larger than the average size. This motivated us to make a comparison between the facet size (Figs. 5 and 12) and the average size of primary α-grains (Fig. 1). Unfortunately, the facet size was 39.4 μm in Fig. 5b while 32.8 μm in Fig. 12a; both are barely different when compared to the average α-grain size of 40.9 ± 12.5 μm. On the contrary, the primary α-grain that led to the fatal-crack initiation seems to be smaller than some grains which are located comparatively closer to the specimen surface, see the overview IPF map in Fig. 6a, 6c, 13a and 13c. Therefore, the combination of larger size and smaller distance-to-surface of the α-grain is unable to explain the facet formation that subsequently triggers the subsurface fatigue cracking as opposed to the surface failure in Ti60 at 450 °C.

Given that all the HCF/VHCF tests were performed using ultrasonic fatigue tester operating at 20 kHz, the possible frequency effect on either the fatigue life or crack initiation mechanism deserves some attention. Papakyriacou et al. [48] compared the room-temperature fatigue behavior of Ti-6Al-7Nb by performing both the 20 kHz and 100 Hz tests. Within the life regime of 10^5 to 2×10^8 cycles, the fatigue data obtained with the rotating bending tester (100 Hz) agreed reasonably well with those generated using the ultrasonic tester (20 kHz). Thus, the frequency effect on the fatigue life was judged as insignificant. Also, SEM fractography examination revealed no difference between the two frequencies, suggesting little frequency effect on the fatigue cracking mechanism of Ti-6Al-7Nb. A similar comment was made regarding the negligible frequency effect based on room-temperature fatigue tests on Ti-6Al-4 V, by comparison of 60 Hz, 400 Hz and 20 kHz in [49], and Ti-6246, by comparison of 20 Hz and 20 kHz in [45].

The only exception in terms of revealing a measurable frequency effect is the work by Takeuchi et al. [50]. They studied the VHCF properties of Ti-6Al-4 V, and tests were performed at frequencies of 120 Hz, 600 Hz, and 20 kHz, respectively. Negligible frequency effect on the fatigue life and crack initiation was found, if the fatal-fatigue cracking occurred from the interior, regardless of testing a smooth or notched bar specimen. But, frequency effect was observed if the fatal-fatigue crack initiated from the surface on the smooth bar specimen, with the high-frequency test led to a higher fatigue strength. Such frequency effect vanished when testing the same material but on the notched bar specimen. They attributed the frequency effect to a delay in local plastic deformation accumulated at the surface of smooth bar specimen in response to high-frequency loading.

Furthermore, a comparative study was conducted by using 100 Hz high-frequency fatigue testers on the present Ti60 at 450 °C. The average fatigue life obtained at the test condition of 100 Hz and 300 MPa

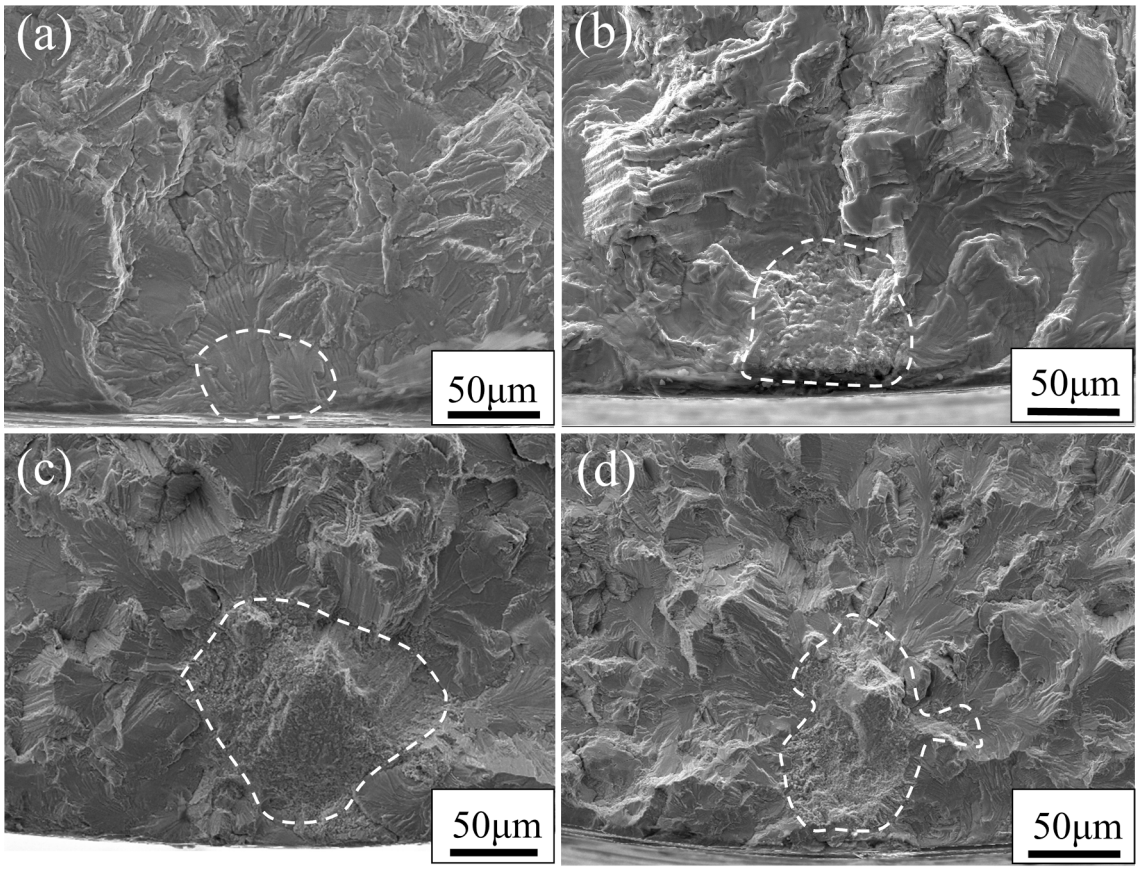

Fig. 11. SEM fractography of HCF/VHCF specimens that received cyclic pre-strain: (a) and (b) surface fatigue-crack initiation, tested at $\sigma_a = 315$ MPa with $N_f = 4 \times 10^4$, and $\sigma_a = 300$ MPa with $N_f = 5.72 \times 10^6$, respectively; (c) and (d) subsurface fatigue-crack initiation tested at $\sigma_a = 280$ MPa with $N_f = 3.02 \times 10^7$, and $\sigma_a = 265$ MPa with $N_f = 1.80 \times 10^8$, respectively. (a) and (c) cyclic pre-straining to 10%, while (b) and (d) to 20% of the LCF life.

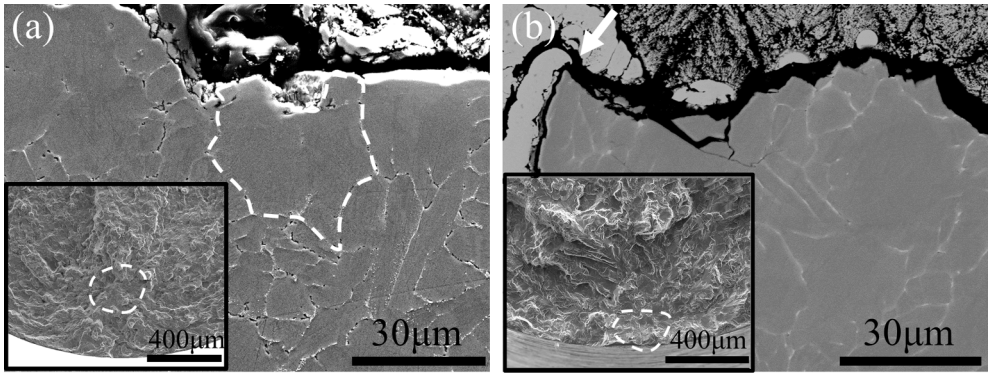

Fig. 12. Longitudinal cross-section of HCF/VHCF fractured specimens that received cyclic pre-strain: (a) subsurface fatigue-crack initiation, $\sigma_a = 300$ MPa, $N_f = 1.53 \times 10^8$; (b) surface fatigue-crack initiation, $\sigma_a = 265$ MPa, $N_f = 8.77 \times 10^6$. The two figure insets provide the SEM fractography revealing the characteristics of the crack initiation region.

was determined as 2.6×10^6 (three tests for each condition), whilst the 20 kHz counterpart provided the fatigue life of 3.2×10^7. This seems to indicate a longer fatigue life of Ti60 with the increased fatigue-loading frequency. A common interpretation is that with the increased loading frequency, dislocations have less time to overcome obstacles via thermal activation, thereby reducing the level of irreversible plastic strain accumulated [51]. However, it is worthwhile to emphasize that the assessment of cyclic pre-strain effect on the Ti60 HCF/VHCF behavior was exclusively based on the ultrasonic fatigue test data. In other words, the presently observed experimental phenomena (surface vs. subsurface cracking and the effect of cyclic pre-strain), are very unlikely to be changed due to the frequency effect.

Regarding the influence of elevated temperature on the surface crack initiation mode, near-α titanium alloys can form oxide layer after exposure at high temperatures of 600 °C and above [12,17,52], with most of the work suggesting a very thin oxide layer developed at 600 °C [17,52]. This means that the observed fatigue crack initiation mode in Ti60 at 450 °C was not related to oxidation. SEM + EDS analysis made on the fracture surface showed no evidence of oxide layer close to the fatigue specimen surface (Fig. S6).

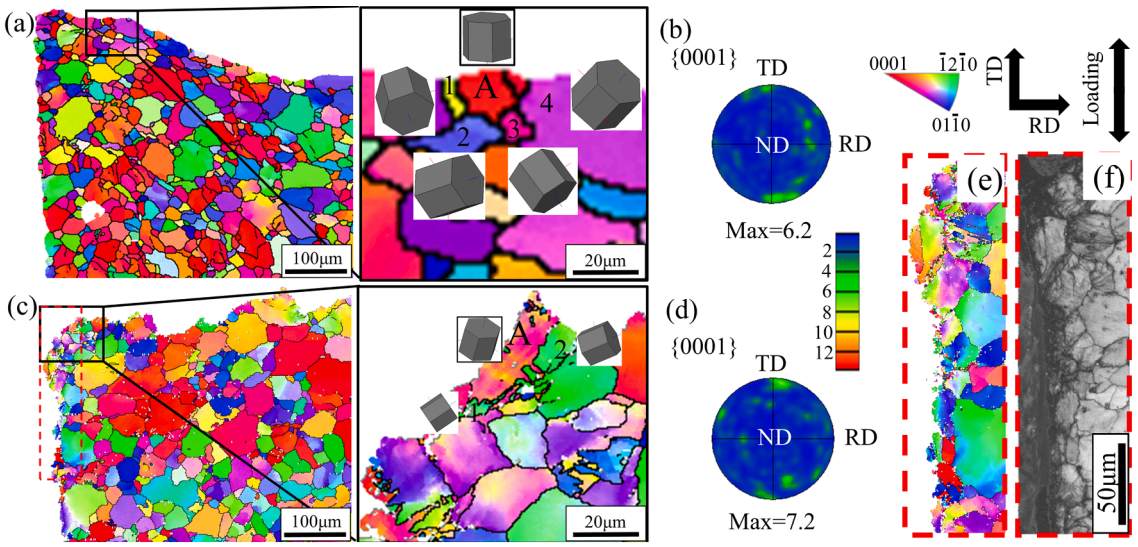

Fig. 13. EBSD cross-sectional observation of the post-fatigued Ti60 that received cyclic pre-strain of ±0.8%: (a) subsurface fatigue-crack initiation, $\sigma_a = 280$ MPa, $N_f = 3.02 \times 10^7$; (c) surface fatigue-crack initiation, $\sigma_a = 280$ MPa, $N_f = 1.39 \times 10^6$. (a) and (c) IPF-TD maps; (b) and (d) {0001} pole figures; and (e) and (f) IPF-TD map and the corresponding band contrast map overlaid with HAGBs for the specimen surface.

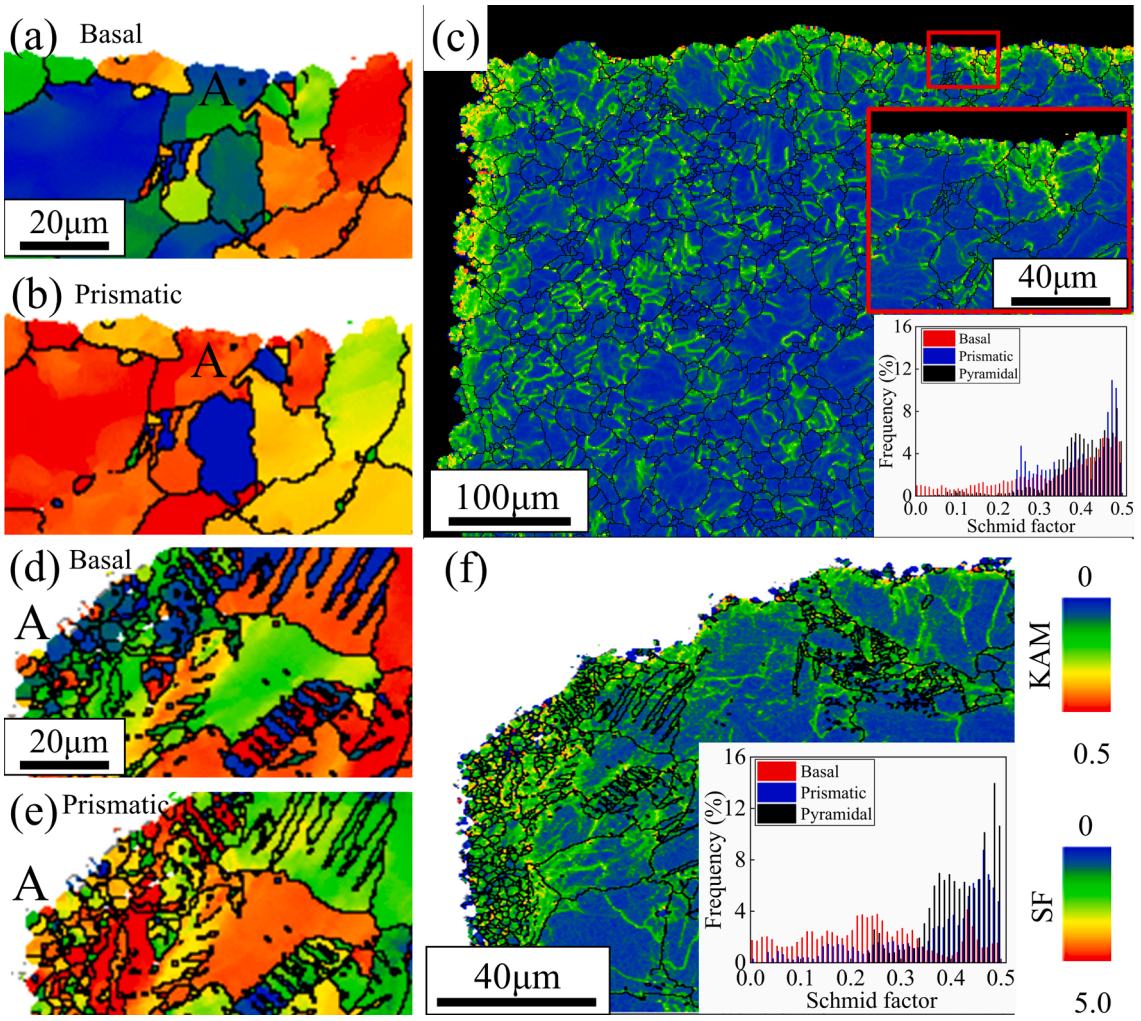

Fig. 14. Kernel average misorientation (KAM), Schmid factor (SF) maps, and their distribution histograms for the no pre-strained specimens: (a) to (c) subsurface fatigue-crack initiation, $\sigma_a = 200$ MPa, $N_f = 3.67 \times 10^8$; (d) to (f) surface fatigue-crack initiation, $\sigma_a = 200$ MPa, $N_f = 6.55 \times 10^6$. (a) and (d) SF of basal < a > slip map while (b) and (e) SF of prismatic < a >. (c) and (f) KAM maps together with the basal < a>, prismatic < a > and pyramidal < c + a > frequency plots shown in the figure inset.

4.2. Local texture vs. overall texture of primary α-grain

The nature of transgranular fracture of α-grain with an hcp crystal structure implies the importance of grain orientation. The pole figures in Fig. 6b and 6d for the no pre-strained Ti60, as well as those in Fig. 13b and 13d for the cyclic pre-strained one, provide evidence for the weak basal texture. By contrast, the critical α-grain A has a considerably high misorientation with reference to its surrounding grains, see the enlarged IPF maps in Fig. 6a, 6c, 13a and 13c. Thus, the present observation in Ti60 supports that the local texture of primary α-grains, instead of the overall texture, plays a predominant role on the fatal-crack initiation at 450 °C under fatigue loading.

Gilbert and Piehler [26] used the selected area channeling pattern and electron channeling contrast imaging to determine the crystallographic orientation of the fracture plane of α-grain linked to the subsurface fatigue-crack initiation in Ti-6Al-4V at room temperature. They concluded that local texture was probably more important than the overall texture, because local alignment of only a few grains in the proper orientation might already enough to trigger the fatal-crack initiation. To visualize the local strain incompatibilities between the particular α-grain and its surrounding regions, the Kernel average misorientation (KAM) and Schmid factor (SF) maps for the three respective slip systems of the basal < a>, prismatic < a > and pyramidal < c + a > have been derived based on the grain orientations in Fig. 6 and Fig. 13. Here, KAM map represents the average misorientation angle of a given point with its three nearest neighbors, and the maximum misorientation in the KAM map was set as 5°, a common value used in the literature (refer to [35,53] for more details). A higher KAM value means a larger local crystal misorientation, indicating a higher plastic strain.

Fig. 14a to 14c as well as the figure inset provide the KAM and SF results for the subsurface cracked Ti60, while Fig. 14d to 14f for the surface cracked Ti60. Both specimens received no cyclic pre-strain. The SF frequency plot shows virtually no difference between the surface and subsurface cracked Ti60, with all three slip systems presenting a fair amount of activity (SF value range from 0.4 to 0.5). In terms of the subsurface cracked Ti60, grain A that formed the transgranular facet shows a much higher intensity of prismatic < a > slip (Fig. 14b) than the basal < a > slip (Fig. 14a). By contrast, most of its neighboring grains have a very low SF intensity for prismatic < a > slip. For grain A, the pyramidal < c + a > SF intensity of 0.47 is as expected because at least five independent slip systems in a polycrystal are required to satisfy the von Mises criterion. In addition, the KAM map shows noticeable local strain concentration in the subsurface crack initiation region as well as the specimen surface.

In terms of the surface cracked Ti60, the SF value of the basal < a> (Fig. 14d), prismatic < a> (Fig. 14e) and pyramidal < c + a > for grain A was measured to be 0.17, 0.45 and 0.47, respectively. But its neighboring grains have a considerably low prismatic < a > slip activation with the SF value ranging from 0.1 to 0.2. The corresponding KAM map in Fig. 14f shows local strain concentration close to the specimen surface. To summarize, the strain incompatibilities exist between the crack-

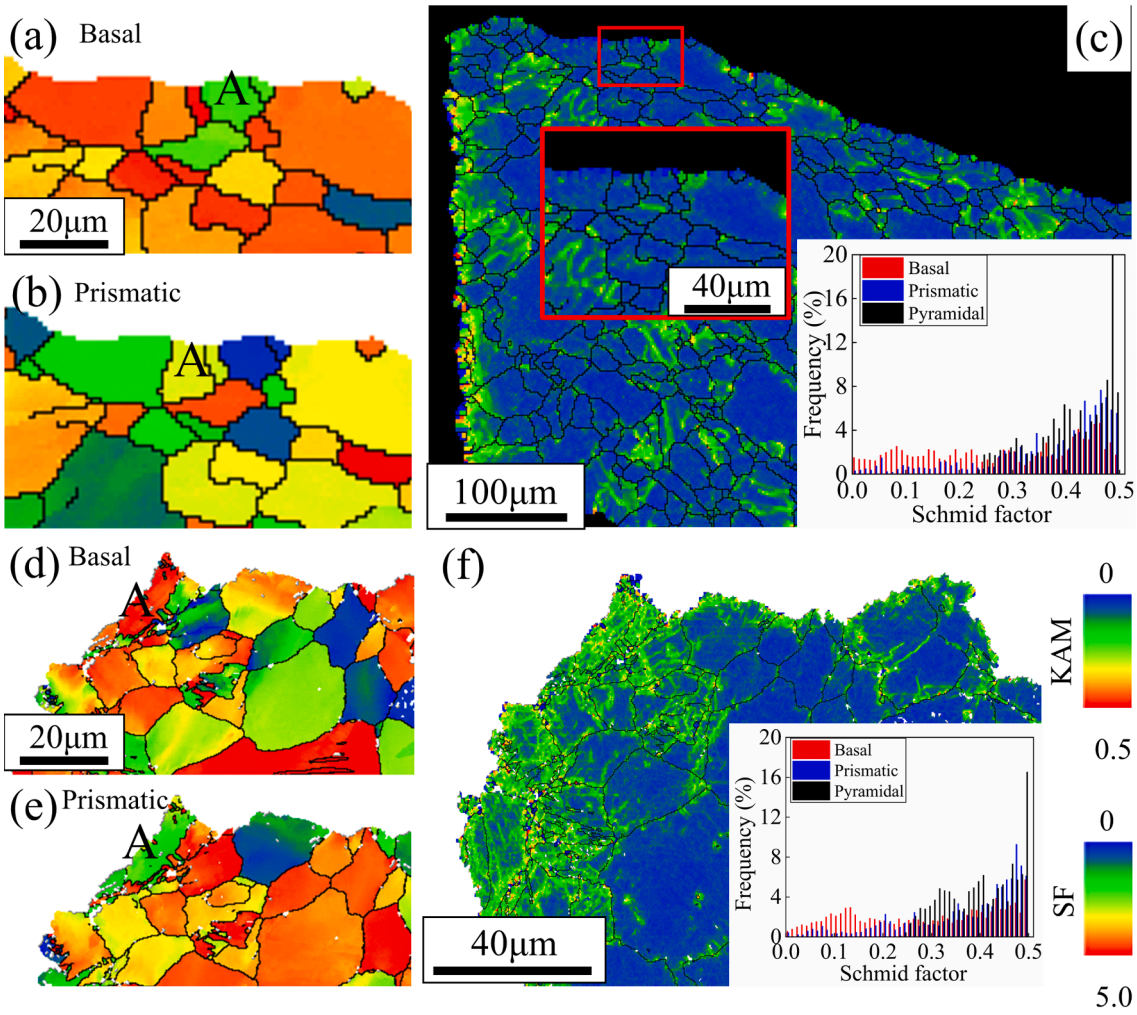

Fig. 15. KAM and SF maps together with their distribution histograms for the cyclic pre-strained specimens under ±0.8%: (a) to (c) subsurface fatigue-crack initiation, $\sigma_a = 280$ MPa, $N_f = 3.02 \times 10^7$; (d) to (f) surface fatigue-crack initiation, $\sigma_a = 280$ MPa, $N_f = 1.39 \times 10^6$.

initiation region and its surroundings, regardless of surface or subsurface fatigue cracking in Ti60 at 450 °C.

For the cyclic pre-strained Ti60, the KAM and SF results for the subsurface cracked specimen are shown in Fig. 15a–c, while the corresponding results for the surface cracked one are presented in Fig. 15d to 15f. All three slip systems have a fair amount of activity. For grain A, the subsurface cracked Ti60 has a very low activity for both the basal < a > and prismatic < a>, but high activity for the pyramidal < c + a>, with their respective SF values of 0.22, 0.03 and 0.50. By contrast, grain A of the surface cracked Ti60 has a high SF value of 0.45 for basal <a>, followed by pyramidal < c + a > of 0.36 and prismatic < a > of 0.19. Again, the activated slip systems in neighbors of grain A are remarkably different from itself, confirming the importance of local texture; this observation applies to both the surface and subsurface cracking scenarios. Local strain concentration was found in the crack initiation site (KAM map), regardless of the surface or subsurface cracking mode.

It may be concluded from the comparison of Fig. 14 (no pre-strain) with Fig. 15 (cyclic pre-strain) that activation of basal < a > slip becomes predominant when the pre-strained Ti60 is subjected to fatigue loading at 450 °C. Also, the fatal-crack initiation is primarily controlled by the local strain concentration. The difference between the two fatigue-crack failure mode lies in that the surface cracked Ti60 exhibits more pronounced surface strain localization when compared to the subsurface cracked one. This implies that the surface strain concentration as manifested by persistent slip bands under fatigue loading is in competition with the local strain concentration in the subsurface due to the misfit strain between a particular α-grain and its nearest neighbors. When the applied stress amplitude is high, Ti60 would be failed by surface cracking as expected. However, the surface strain concentration is not high enough to trigger the surface cracking when the stress amplitude is considerably low. This can satisfactorily explain why subsurface cracking is exclusively found in the VHCF regime (i.e. $N_f > 10^7$), Fig. 10.

In addition, observations based on four individual fractured α-grains indicate that the fracture plane is not necessarily a basal type in Ti60 at 450 °C (i.e. basal plane fracture in Fig. 13a, while prismatic, pyramidal or other non-basal types in Fig. 6a, 6c and 13c). This finding is consistent with the previous HCF work at room temperature on β-annealed Ti-6Al-4V [54] showing the α-phase cracking on a prismatic plane, on Ti-6Al-4V with bi-modal microstructure showing the α-phase cracking on a pyramidal plane [26], on Ti-6Al-4V [20] showing a basal plane cracking, on a near-α IMI685 [55] showing a pure basal fracture, and on Ti-6242 [5] showing the fracture plane oriented less than 5° with respect to the basal plane.

4.3. Effect of pre-strain

It is evident that cyclic pre-strain helps to enhance the Ti60 fatigue strength by 100 MPa, Fig. 10. The main contribution of LCF pre-straining is to create a cyclically hardened Ti60 (Fig. 8a). Many dislocations would be generated prior to the subsequent HCF/VHCF loading, and they can influence one another through their strain fields, leading to the pinning effect to prevent further dislocation movement, especially at a considerably reduced stress amplitude. In this context, the improved HCF/VHCF performance of the pre-strained Ti60 can be solely attributed to the cyclic strain hardening.

For the titanium alloys, the effect of LCF pre-straining at elevated temperatures on the subsequent HCF/VHCF life has yet to be explored in previous work. But the literature survey conducted by us regarding the pre-strain effect on room-temperature fatigue of titanium alloys shed some important light on why a beneficial pre-strain effect was observed in the present Ti60 at 450 °C. First, the room-temperature LCF resistance of commercially-pure Ti was remarkably improved with increasing the volume fraction of deformation twins, but they can also lead to accumulation of fatigue damage depending on their amount [56]. By studying the same material, Chang et al. [57] reported that the detrimental effect of pre-strain up to 8% on the subsequent LCF life was more pronounced at low strain amplitudes. This was attributed to the irreversibility of dislocation structures inherited from the pre-strain. At high strain amplitude, the pre-strain induced dislocation structures can be erased completely during the subsequent LCF testing, resulting in no pre-strain effect.

Second, effect of LCF on HCF strength was studied on Ti-6Al-4V at room temperature by Mall et al. [58] and Lanning et al. [59], respectively. The former study revealed no statistically significant effect of the prior LCF pre-strain (up to 50% of expected LCF life) on the subsequent HCF strength. The latter work found that LCF loading, applied for 75% of the LCF life resulted in only small reductions in the subsequent HCF strength. Third, Golland and Beevers [60] concluded that the lowering of the room-temperature fatigue strength of α-Ti following tensile pre-straining depended on the effects of dislocation unpinning, twin-assisted fatigue damage and intergranular cracking induced by the level and temperature of the pre-strain.

The aforementioned work suggests the competition existing between the deformation and damage induced by pre-straining. Regarding the fatigue damage, the two evidence as follows supporting the absence of damage caused by LCF pre-straining up to 20% of the life in Ti60. First, there was small difference of the *b* value (Fatigue strength exponent in Table 2) between the no pre-strained and pre-strained Ti60. Second, the difference of the elastic moduli between the tension- and compression-going phases of the fatigue cycle only increased significantly after 80% of the LCF life. Fig. 9b. Therefore, the cyclic pre-strain up to 20% of the LCF life is expected to generate the beneficial effect on the subsequent HCF strength of Ti60. An immediate question might arise as to whether an increased proportion of the LCF life (i.e. >20% but up to the maximum peak stress magnitude, Fig. 8a) would achieve a further enhanced HCF strength. According to two HCF studies [61] on steels involving the room-temperature pre-straining, it may be deduced that if the dislocation cell structure is not developed, at least no detrimental effect should be expected regarding the cyclic pre-straining on Ti60. This is because with further pre-straining, the improving tendency would be reduced eventually, due to the combined effects of deformation homogeneity and reversibility.

The S-N curve duality as observed in the cyclic pre-strained Ti60 can be understood by accepting the fact that the local primary α-grain texture would not be easily altered, at least not to a great extent, by just receiving a cyclic pre-straining up to 20% of the LCF life. Our EBSD-based slip system analysis performed on the post-VHCF Ti60 seems to indicate that prismatic < a > slip is more active than basal < a > slip in the no cyclic pre-strained Ti60, see the SF distribution histograms in Figs. 14 and 15. It is thus hypothesized that a great number of grains would be subjected to a prismatic < a > slip during LCF pre-straining. To test this hypothesis, TEM dislocation observation was performed on three sample conditions: as-received Ti60, cyclic pre-strained to 10% and 20% of the LCF life, respectively.

All TEM images were taken along the same zone axis of $[2\bar{1}\bar{1}0]$ to ensure a like-for-like comparison [62], with the diffraction vector of $\boldsymbol{g}(01\bar{1}1)$ indicated. Fig. 16a presents a TEM bright-field image of the Ti60 receiving no pre-strain. It is interesting, though, to see the slip bands, which is most likely due to the material processing history. The corresponding SAD taken from the same area as the TEM imaging confirms that such slip bands are nearly parallel to the $\{0\bar{1}12\}$ plane. By using the same approach, the slip bands induced by the LCF pre-straining are nearly aligned to the $\{10\bar{1}0\}$ plane for both the 10% and 20% test conditions (Fig. 16b and 16c). Therefore, we may conclude that the deformation mechanism during the cyclic pre-strain is dominated by the prismatic < a > slip, and in turn, our hypothesis based on the EBSD slip systems (Figs. 14 and 15) is valid.

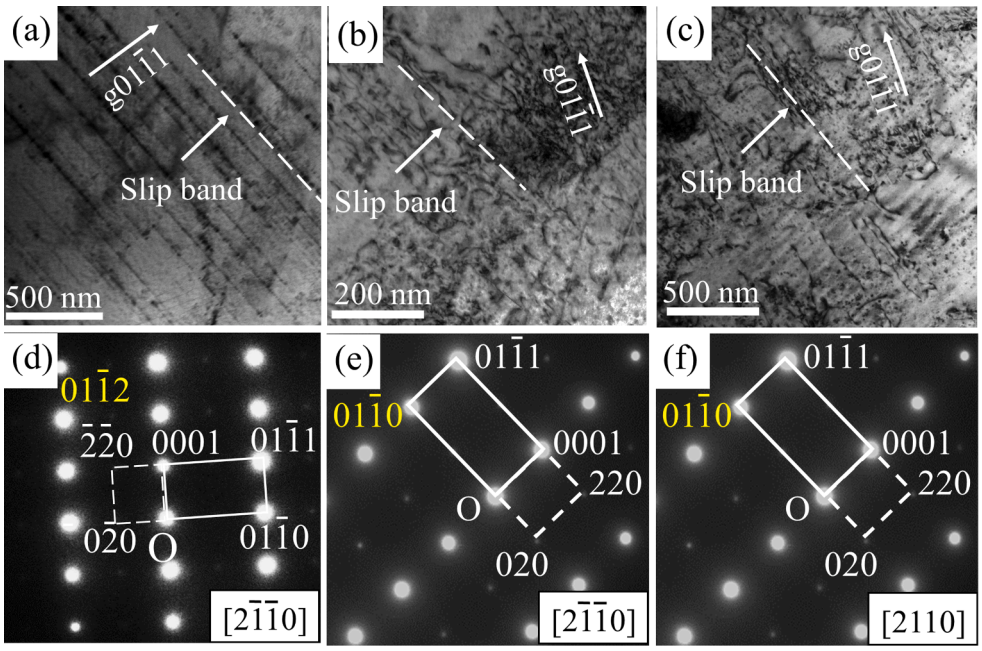

Fig. 16. TEM bright-field images in (a) to (c) and corresponding SADs in (d) to (f). No pre-strained Ti60 in (a), cyclic pre-strained to 10% of LCF life in (b), and cyclic pre-strained to 20% of LCF life in (c).

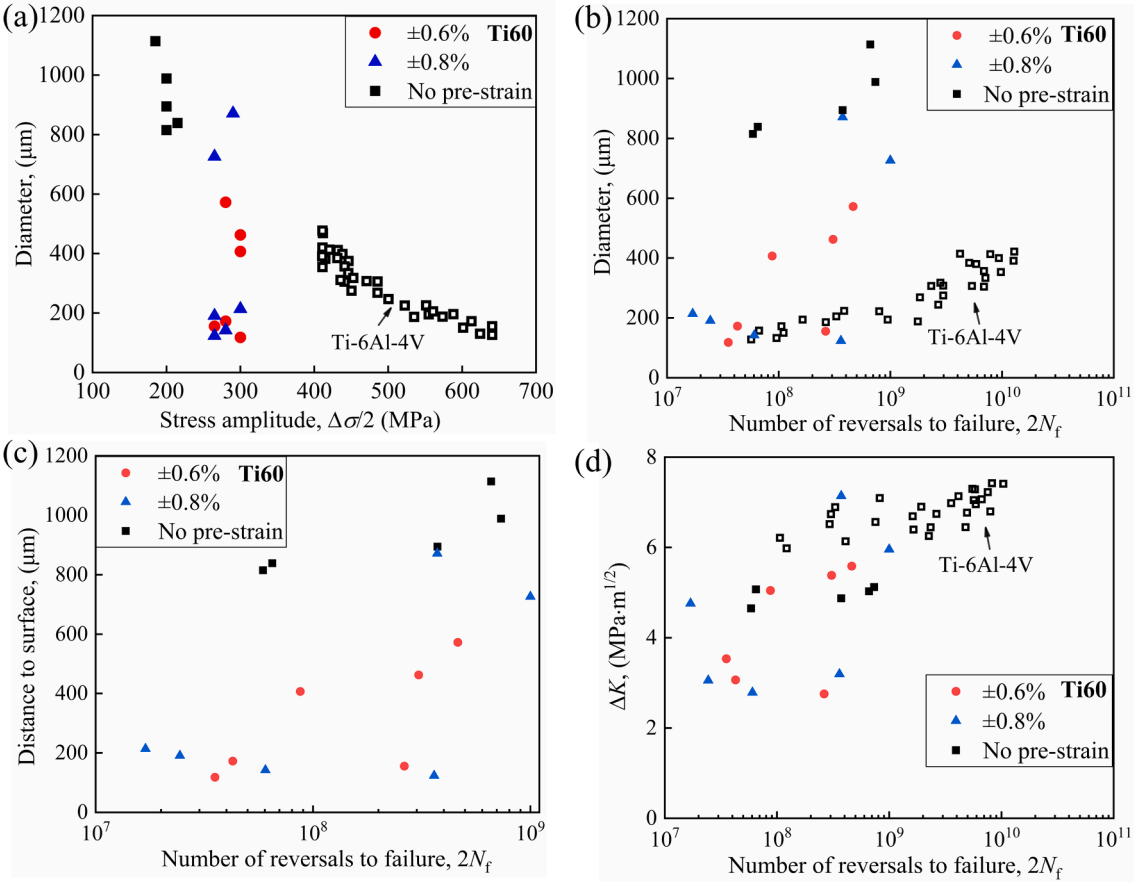

Fig. 17. Dependence of the rough zone as observed in the crack initiation site of Ti60: diameter of the rough-zone area plotted as a function of stress amplitude in (a) and fatigue life in (b); distance of the rough zone to specimen surface plotted as a function of fatigue life in (c); stress intensity factor amplitude around the rough zone vs. fatigue life in (d). Note that Ti-6Al-4 V data obtained by room temperature fatigue was .
adapted from [22]

4.4. Rough zone

The fracture surfaces of the Ti60 tested in the VHCF regime, especially for those failed by the subsurface cracking mode, are characterized by a rough zone within the crack initiation site, see Fig. 4b, 5a, 11c, 11d, S4b, S5b and S5d. The center of the rough zone seems to be the primary α-grain facet. Note that the presence of rough zone is not exclusive to the subsurface cracked Ti60. It can also be found in the surface cracked Ti60, e.g. Fig. 11b and refer to Table S2 for the full detail. But there is evidence to suggest that all the surface cracked Ti60 with the rough-zone characteristics tends to have a fatigue life of between 10^6 and 10^7, and hence not far from the VHCF regime.

The rough zone as revealed in the SEM fractography of the crack initiation site was reported previously by Zuo et al. [23] while studying the room-temperature VHCF behavior of Ti-6Al-4V with bi-modal microstructure, by Pan et al. [Ref. in response 1–5] while investigating the room-temperature VHCF behavior of TC4 (the Chinese version of Ti-6Al-4V) with equiaxed microstructure, and by Heinz and Eifler [22] while studying VHCF behavior of Ti-6Al-4V at room temperature. Especially, the term optical dark area (ODA) was used to describe this interesting crack-initiation feature [22]. A clear correlation was identified between the stress amplitude, fatigue cycles and the ODA size. At the highest stress amplitude, the smallest diameter of the ODA was observed. To investigate whether a similar correlation between the size of rough zone and fatigue stress exists in the present Ti60, the equivalent diameter of the rough-zone area was quantified and tabulated in Table S2.

Fig. 17a presents the measured diameter of rough zone formed in Ti60 against the stress amplitude. Although a general trend suggests the diameter is reduced with the increasing stress amplitude, its rate of change seems to be very steep, indicating an unrealistic strong stress dependence. Future work is required to validate whether this is true. For comparison purposes, the Ti-6Al-4V room-temperature fatigue results showing the dependence of the diameter of ODA on the stress amplitude is given in Fig. 17a. Similarly, the diameter of the rough zone seems to have a positive correlation with the fatigue cycles to failure in Ti60, Fig. 17b. But, again, the large data scatter does not permit us to draw an unambiguous conclusion. This is particularly the case when compared to the room-temperature fatigue on Ti-6Al-4V. A question might arise as to whether the distance-to-surface would help to reconcile the rough-zone observation. Unfortunately, Heinz and Eifler [22] did not report the individual data of the distance of ODA to surface. Hence, we could not include their data to make a comparison. Fig. 17c shows the relationship of the rough-zone distance to specimen surface plotted against the fatigue life. Again, only a general trend can be noticed with a positive correlation.

The stress intensity factor amplitude around the rough zone, ΔK, was calculated following equation proposed by Murakami et al. [63,64].

$$\Delta K = A(\Delta\sigma/2)\sqrt{\pi\sqrt{area}} \quad (1)$$

where the shape factor A was taken as 0.5 for the case of internal crack initiation as opposed to the value of 0.65 for the near-to-surface one. A similar approach was successfully adopted in our previous VHCF work on Ni-base superalloy when considering casting pore [31]. Fig. 17d presents the relationship between ΔK and fatigue life. The large data scatter for the Ti60 at 450 °C does not permit us to draw any conclusion. By contrast, the Ti-6Al-4V result seems to give a lower data scatter, despite an almost constant ΔK value when plotted against N_f.

4.5. Summary: Ti60 vs. IMI834

It is generally accepted that the most influential microstructural parameter on the mechanical properties of bi-modal microstructures in titanium alloys is the relatively small β-grain size [2]. The β-grain size is about equal to the distance between the primary α-grains, and thus both the volume fraction and size of primary α-grains play a key role in determining the effective slip length of dislocations. The volume fraction of primary α-grains in the present Ti60 was measured to be 23.5% (Fig. 1), which is higher than that of 14% in [14], 18% in [7], and 10–15% in [65] for IMI834, but similar to that of 25% in [15] for IMI834. In terms of the average size of primary α-grains, Ti60 had a value of 40.9 ± 12.5 μm, which is significantly higher than 14 μm in [7] and 25 μm in [15] for IMI834. This explains reasonably well about the large lamellar transformed-β matrix in Ti60 with an average grain size of 63.2 ± 8.9 μm. By contrast, the lamellar transformed-β grain size was reported as 25 μm in [7] and less than 50 μm in [15] for IMI834. Given a similar 450 °C LCF properties between the Ti60 (increased Si concentration and Ta addition) and IMI834, Fig. 7, the present results suggest that the Ti60 microstructure control is needed, presumably by adopting a faster cooling rate from the homogenization temperature in the β-phase field, in a combination with the adjustment of recrystallisation temperature after the deformation processing step. This favors the formation of finer primary α-grains with lower volume fraction as well as the refined β-grains. This holds the promise in further enhancing the fatigue properties of Ti60 at 450 °C.

5. Conclusions

The following conclusions can be drawn based on the 450 °C VHCF study of a near-α titanium alloy in both the cyclic pre-strained and no pre-strained conditions.

(1) S-N curve duality appears in Ti60 with bi-modal microstructure, regardless of cyclic pre-strain condition. Cyclic pre-strain up to a level of 10% of the LCF life can result in fatigue strength enhancement of up to 100 MPa.
(2) During VHCF loading, the surface strain concentration is in competition with the local strain concentration in the subsurface due to the misfit strain between the particular α-grain and its nearest neighbors. This can provide plausible explanation about the random switch between the surface and subsurface cracking when the level of stress results in a fatigue life close to the borderline between the HCF and VHCF regime (10^7 cycles).
(3) The local texture is more important than the overall texture because it is the misfit strain induced by the high misorientation of a particular primary α-grain that determines the subsurface fatigue-crack initiation.
(4) At high fatigue stress, all Ti60 specimens exhibit a surface fatigue cracking, while an exclusively subsurface fatigue cracking scenario is found when the fatigue stress is considerably low, i.e. within the VHCF regime.

6. Data availability statement

The raw data required to reproduce these findings are available upon a reasonable request. Please directly contact the corresponding author of this paper.

CRediT authorship contribution statement

Z. Zhao: Conceptualization, Supervision, Funding acquisition. **R. Zhou:** Investigation, Writing – original draft, Formal analysis, Visualization. **Z. Wang:** Investigation, Formal analysis. **J. Cai:** Investigation, Resources. **B. Chen:** Conceptualization, Supervision, Writing – original draft, Writing – review & editing.

Declaration of Competing Interest

The authors declare that they have no known competing financial interests or personal relationships that could have appeared to influence the work reported in this paper.

Acknowledgement

Zihua Zhao acknowledges financial supports by the National Natural Science Foundation of China (91860110, 51571009) and the National Science and Technology Major Project of China (J2019-VI-0022-0138). Bo Chen acknowledges financial supports by the UK's Engineering and Physical Sciences Research Council, through the Early Career Fellowship Scheme EP/R043973/1. In addition, Bo Chen extends his sincere thank you to Prof. Shengkai Gong at Beihang University to promote this international research collaboration.

Appendix A. Supplementary material

Supplementary data to this article can be found online at https://doi.org/10.1016/j.ijfatigue.2022.106918.

References

[1] Sharma H, Parfitt D, Syed AK, Wimpenny D, Muzangaza E, Baxter G, et al. A critical evaluation of the microstructural gradient along the build direction in electron beam melted Ti-6Al-4V alloy. Materials Science and Engineering A 2019;744:182–94.
[2] Lutjering G, Williams JC. Titanium. 2nd ed. Springer; 2007.
[3] Rosenberg HW. The Science, Technology and Application of Titanium. Oxford, UK, (1970) p. 851-859: Pergamon Press; n.d.
[4] Collings EW. Materials Properties Handbook: Titanium Alloys. USA: Materials Park; 1994.
[5] Sinha V, Mills MJ, Williams JC. Crystallography of fracture facets in a near-alpha titanium alloy. Metall Mater Trans A 2006;37(6):2015–26.
[6] Singh N, Gouthama, Singh V. Low cycle fatigue behaviour of Ti alloy Timetal 834 at 873 K. Int J Fatigue 2007;29(5):843–51.
[7] Hardt S, Maier HJ, Christ HJ. High-temperature fatigue damage mechanisms in near-α titanium alloy IMI 834. Int J Fatigue 1999;21:779–89.
[8] Peng W, Zeng W, Wang Q, Yu H. Characterization of high-temperature deformation behavior of as-cast Ti60 titanium alloy using processing map. Materials Science and Engineering A 2013;571:116–22.
[9] Jia W, Zeng W, Zhou Y, Liu J, Wang Q. High-temperature deformation behavior of Ti60 titanium alloy. Mater Sci Eng, A 2011;528(12):4068–74.
[10] Cai J, Huang X, Ma J, Cao C. Compositional optimization of advanced high temperature titanium alloys under guidance of phase diagram and diffusion theory. Rare Met 2009;28:238–41.
[11] Tabie VM, Li C, Saifu W, Li J, Xu X. Mechanical properties of near alpha titanium alloys for high-temperature applications - a review. Aircraft Engineering and Aerospace Technology 2020;92(4):521–40.
[12] Sai Srinadh KV, Singh V. Oxidation behaviour of the near α-titanium alloy IMI 834. Bull Mater Sci 2004;27(4):347–54.
[13] Prasad K, Sarkar R, Kumar V, Rao KBS, Sundararaman M. Influence of test temperature on cyclic deformation behavior of a near α titanium alloy. Mater Sci Eng, A 2016;662:373–84.
[14] Singh N, Gouthama, Singh V. Low cycle fatigue behavior of Ti alloy IMI 834 at room temperature. Mater Sci Eng, A 2002;325(1-2):324–32.
[15] Kordisch T, Nowack H. Life prediction for the titanium alloy IMI 834 under high temperature creep-fatigue loadings. Fatigue Fract Eng Mater Struct 1998;21(1):47–63.
[16] Prasad K, Abhaya S, Amarendra G, Kumar V, Rajulapati KV, Rao BS, et al. Fatigue crack growth behaviour of a near α titanium alloy Timetal 834 at 450°C and 600°C. Eng Fract Mech 2013;102:194–206.
[17] Jia W, Zeng W, Zhang X, Zhou Y, Liu J, Wang Q. Oxidation behavior and effect of oxidation on tensile properties of Ti60 alloy. J Mater Sci 2011;46(5):1351–8.
[18] Yokoyama H, Umezawa O, Nagai K, Suzuki T. Distribution of internal crack initiation sites in high-cycle fatigue for titanium alloys. ISIJ Int 1997;37:1237–44.
[19] Tokaji K, Ohya K, Kariya H. Subsurface fatigue crack initiation in beta titanium alloys. Fatigue Fract Eng Mater Struct 2000;23(9):759–66.
[20] Neal DF, Blenkinsop PA. Internal fatigue origins in alpha-beta titanium alloys. Acta Metall 1976;24:59–63.
[21] Ravi Chandran KS, Jha SK. Duality of the S-N fatigue curve caused by competing failure modes in a titanium alloy and the role of Poisson defect statistics. Acta Mater 2005;53(7):1867–81.
[22] Heinz S, Eifler D. Crack initiation mechanisms of Ti6Al4V in the very high cycle fatigue regime. Int J Fatigue 2016;93:301–8.
[23] Zuo JH, Wang ZG, Han EH. Effect of microstructure on ultra-high cycle fatigue behavior of Ti-6Al-4V. Mater Sci Eng, A 2008;473(1-2):147–52.
[24] McEvily AJ, Nakamura T, Oguma H, Yamashita K, Matsunaga H, Endo M. On the mechanism of very high cycle fatigue in Ti-6Al-4V. Scr Mater 2008;59(11):1207–9.
[25] Li W, Li M, Sun R, Xing X, Wang P, Sakai T. Faceted crack induced failure behavior and micro-crack growth based strength evaluation of titanium alloys under very high cycle fatigue. Int J Fatigue 2020;131(105369):1–11.
[26] Gilbert JL, Piehler HR. On the nature and crystallographic orientation of subsurface cracks in high cycle fatigue of Ti-6Al-4V. Metall Trans A 1993;24(3):669–80.
[27] Sinha V, Mills MJ, Williams JC, Spowart JE. Observations on the faceted initiation site in the dwell-fatigue tested Ti-6242 alloy: Crystallographic orientation and size effects. Metall Mater Trans A 2006;37(5):1507–18.
[28] Chandravanshi V, Prasad K, Singh V, Bhattacharjee A, Kumar V. Effects of α + β phase deformation on microstructure, fatigue and dwell fatigue behavior of a near alpha titanium alloy. Int J Fatigue 2016;91:100–9.
[29] Wang R-Z, Bo-Chen, Zhang X-C, Tu S-T, Ji-Wang, Zhang C-C. The effects of inhomogeneous microstructure and loading waveform on creep-fatigue behaviour in a forged and precipitation hardened nickel-based superalloy. Int J Fatigue 2017;97:190–201.
[30] Yuan G, Zhang X, Chen B, Tu S, Zhang C. Low-cycle fatigue life prediction of a polycrystalline nickel-base superalloy using crystal plasticity modelling approach. J Mater Sci Technol 2020;38:28–38.
[31] Zhao Z, Zhang F, Dong C, Yang X, Chen B. Initiation and early-stage growth of internal fatigue cracking under very-high-cycle fatigue regime at high temperature. Metall Mater Trans A 2020;51(4):1575–92.
[32] Zhao Z, Li Q, Zhang F, Xu W, Chen B. Transition from internal to surface crack initiation of a single-crystal superalloy in the very-high-cycle fatigue regime at 1100 °C. Int J Fatigue 2021;150(106343):1–14.
[33] Zhao Z, Liang Z, Li Q, Zhang F, Chen B. Crack initiation and propagation behaviour under high-temperature very-high-cycle fatigue: Directionally solidified columnar-grained vs. single-crystal superalloys. Mater Sci Eng, A 2022;836:142711.
[34] Zhao P, Chen B, Zheng Z, Guan B, Zhang X, Tu S. Microstructure and texture evolution in a post-dynamic recrystallised titanium during annealing, monotonic and cyclic loading. Metall Mater Trans A 2021;52:394–412.
[35] Li Y, Parfitt D, Flewitt PEJ, Hou X, Quinta de Fonseca J, Chen B. Microstructural considerations of enhanced tensile strength and mechanical constraint in a copper/stainless steel brazed joint. Mater Sci Eng, A 2020;796(139992):1–13.
[36] Jin J, Gao R, Peng H, Guo H, Gong S, Chen B. Rapid Solidification Microstructure and Carbide Precipitation Behavior in Electron Beam Melted High-Speed Steel. Metall Mater Trans A 2020;51(5):2411–29.
[37] Kan W, Chen B, Peng H, Liang Y, Lin J. Formation of columnar lamellar colony grain structure in a high Nb-TiAl alloy by electron beam melting. J Alloy Compd 2019;809(151673):1–14.
[38] Williams DB, Carter CB, editors. Transmission Electron Microscopy. Boston, MA: Springer US; 2009.
[39] Bonnet R, Cousineau E, Warrington DH. Determination of near-coincident cells for hexagonal crystals. Related DSC lattices. Acta Crystallographica Section A 1981;37(2):184–9.
[40] Stanford N, Carlson U, Barnett MR. Deformation Twinning and the Hall–Petch Relation in Commercial Purity Ti. Metall and Mat Trans A 2008;39(4):934–44.
[41] Wu L, Jain A, Brown DW, Stoica GM, Agnew SR, Clausen B, et al. Twinning – detwinning behavior during the strain-controlled low-cycle fatigue testing of a wrought magnesium alloy, ZK60A. Acta Mater 2008;56(4):688–95.
[42] Gao PF, Lei ZN, Li YK, Zhan M. Low-cycle fatigue behavior and property of TA15 titanium alloy with tri-modal microstructure. Mater Sci Eng, A 2018;736:1–11.
[43] Zhang SQ, Li SJ, Jia MT, Prima F, Chen LJ, Hao YL, et al. Low-cycle fatigue properties of a titanium alloy exhibiting nonlinear elastic deformation behavior. Acta Mater 2011;59(11):4690–9.
[44] Wang H, Sun QY, Xiao L, Sun J, Ge P. Low-cycle fatigue behavior and deformation substructure of Ti-2Al-2.5Zr alloy at 298 and 673K. Mater Sci Eng, A 2010;527(15):3493–500.
[45] Szczepanski CJ, Jha SK, Larsen JM, Jones JW. Microstructural influences on very-high-cycle fatigue-crack initiation in Ti-6246. Metall Mater Trans A 2008;39(12):2841–51.
[46] Bridier F, Villechaise P, Mendez J. Analysis of the different slip systems activated by tension in a α/β titanium alloy in relation with local crystallographic orientation. Acta Mater 2005;53(3):555–67.
[47] Bridier F, Villechaise P, Mendez J. Slip and fatigue crack formation processes in an α/β titanium alloy in relation to crystallographic texture on different scales. Acta Mater 2008;56(15):3951–62.
[48] Papakyriacou M, Mayer H, Pypen C, Plenk H, Stanzl-Tschegg S. Influence of loading frequency on high cycle fatique properties of b.c.c and h.c.p. metals. Mater Sci Eng, A 2001;308:143–52.
[49] Morrissey R, Nicholas T. Fatigue strength of Ti-6Al-4V at very long lives. Int J Fatigue 2005;27(10-12):1608–12.
[50] Takeuchi E, Furuya Y, Nagashima N, Matsuoka S. The effect of frequency on the giga-cycle fatigue properties of a Ti-6Al-4V alloy. Fatigue Fract Eng Mater Struct 2008;31:599–605.
[51] Morrissey RJ, McDowell DL, Nicholas T. Frequency and stress ratio effects in high cycle fatigue of Ti-6Al-4V. Int J Fatigue 1999;21:679–85.
[52] Guleryuz H, Cimenoglu H. Oxidation of Ti-6Al-4V alloy. J Alloy Compd 2009;472(1-2):241–6.
[53] Miao J, Pollock TM, Wayne Jones J. Microstructural extremes and the transition from fatigue crack initiation to small crack growth in a polycrystalline nickel-base superalloy. Acta Mater 2012;60(6-7):2840–54.
[54] Ruppen JA, Eylon D, McEvily AJ. Subsurface fatigue crack initiation of β-annealed Ti-6Al-4V. Metall Trans A 1980;11(6):1072–5.
[55] Davidson DL, Eylon D. Titanium alloy fatigue fracture facet investigation by selected area electron channeling. Metall Trans A 1980;11(5):837–43.
[56] Kim G, Shams SAA, Kim JN, Won JW, Choi SW, Hong JK, et al. Enhancing low-cycle fatigue life of commercially-pure Ti by deformation at cryogenic temperature. Mater Sci Eng, A 2021;803:140698.
[57] Chang Le, Ma T-H, Wen J-B, Zhou B-B, Li J, He X-H, et al. The distinct influences of pre-strain on low cycle fatigue behavior of CP-Ti along rolling direction at different strain amplitudes. Mater Sci Eng, A 2019;763:138150.

[58] Mall S, Nicholas T, Park TW. Effect of predamage from low cycle fatigue on high cycle fatigue strength of Ti-6Al-4V. Int J Fatigue 2003;25:1109–16.
[59] Lanning D, Haritos GK, Nicholas T, Maxwell DC. Low-cycle fatigue / high-cycle fatigue interactions in notched Ti – 6Al – 4V. Fatigue Fract Eng Mater Struct 2001; 24(9):565–77.
[60] Golland DI, Beevers CJ. Some effects of prior deformation and annealing on the fatigue response of α-titanium. Journal of The Less-Common Metals 1971;23(1): 53–60.
[61] Kim S, Song T, Sung H, Kim S. Effect of pre-straining on high cycle fatigue and fatigue crack propagation behaviors of complex phase steel. Met Mater Int 2021;27 (10):3810–22.
[62] Cizek P, Kada SR, Wang J, Armstrong N, Antoniou RA, Lynch PA. Dislocation structures representing individual slip systems within the α phase of a Ti–6Al–4V alloy deformed in tension. Mater Sci Eng, A 2020;797:140225.
[63] Murakami Y, Kodama S, Konuma S. Quantitative evaluation of effects of non-metallic inclusions on fatigue strength of high strength steels. I: Basic fatigue mechanism and evaluation of correlation between the fatigue fracture stress and the size and location of non-metallic inclusions. Int J Fatigue 1989;11(5):291–8.
[64] Murakami Y, Endo M. Effects of defects, inclusions and inhomogeneities on fatigue strength. Int J Fatigue 1994;16(3):163–82.
[65] Radecka A, Coakley J, Vorontsov VA, Martin TL, Bagot PAJ, Moody MP, et al. Precipitation of the ordered α_2 phase in a near-α titanium alloy. Scr Mater 2016; 117:81–5.